

2008

Comparative study of a nearbody flowfield application of three particle image diagnostic techniques

Abhishek Bichal
University of Dayton

Follow this and additional works at: https://ecommons.udayton.edu/graduate_theses

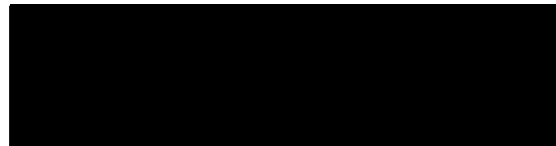
Recommended Citation

Bichal, Abhishek, "Comparative study of a nearbody flowfield application of three particle image diagnostic techniques" (2008). *Graduate Theses and Dissertations*. 1546.
https://ecommons.udayton.edu/graduate_theses/1546

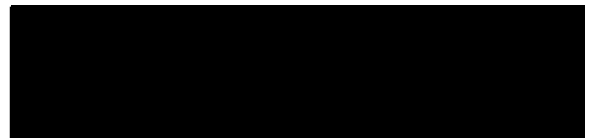
This Thesis is brought to you for free and open access by the Theses and Dissertations at eCommons. It has been accepted for inclusion in Graduate Theses and Dissertations by an authorized administrator of eCommons. For more information, please contact mschlangen1@udayton.edu, ecommons@udayton.edu.

COMPARATIVE STUDY OF A NEARBODY FLOWFIELD APPLICATION OF
THREE PARTICLE IMAGE DIAGNOSTIC TECHNIQUES

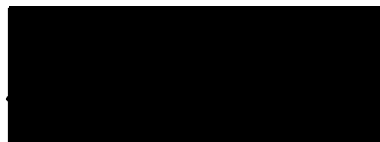
APPROVED BY:



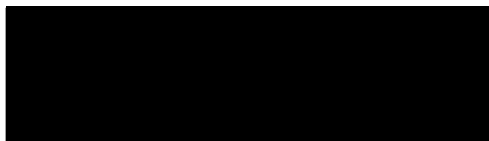
Aaron Altman, Ph.D.,
Advisory Committee Chairman
Assistant Professor, Mechanical and
Aerospace Engineering Department



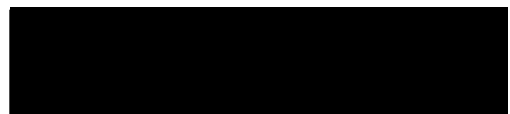
John Petrykowski, Ph.D.,
Committee Member
Associate Professor, Mechanical and
Aerospace Engineering Department



Jordi Estevadeordal, Ph.D.,
Advisory Committee Member,
Innovative Scientific Solutions, Incorporated



Malcolm W. Daniels, Ph.D.,
Associate Dean,
School of Engineering



Joseph E. Saliba, Ph.D., P.E.
Dean, School of Engineering

©Copyright
Abhishek Bichal
All right reserved
2008

ABSTRACT

COMPARATIVE STUDY OF A NEARBODY FLOWFIELD APPLICATION OF THREE PARTICLE IMAGE DIAGNOSTIC TECHNIQUES

Name: Bichal, Abhishek

University of Dayton

Advisor: Dr. Aaron Altman

A comparative study to determine the applicability of three Particle Image Diagnostic Techniques (PIDT's) for near body flow diagnostics at small Fields Of View (FOV), and large Reynolds Number (Re), 22000 (with respect to the 14.3 mm diameter of the particulate sampling probe), and the challenges associated with each technique were studied. Very few studies have been performed comparing the relative performance of different PIDT's applied to the same problem in order to benchmark the different methods. In this study, three PIDT's, Particle Shadow Velocimetry (PSV), Volume Illuminated Forward Scatter Particle Image Velocimetry (VIFS-PIV) and Particle Image Velocimetry (PIV), were used to study the near body flow field of a particulate sampling probe. This flow diagnostic study in the University of Dayton Low Speed Wind Tunnel also complemented the validation of a computational investigation performed at the US Air Force Research Laboratory Propulsion Directorate. In the PSV experiments, the flow was seeded with either the talc, glass balloons or phenolic resin. The large particle size and the large seed material density gave biased results from the experiments. Smoke was used to seed the flow in both variants of

ACKNOWLEDGEMENTS

My special thanks and gratitude are in order to my advisor Dr. Aaron Altman for both his emotional and financial support, and for the many hours he spent in guiding, advising and directing this project. He was greatly instrumental in my bringing this thesis to a conclusion with his patience and expertise.

I want to thank Dr. Jordi Estevadeordal, Innovative Scientific Solutions, Incorporated, for his technical advice and for the laser through a CRADA program from AFRL which was instrumental in this project. I want to thank Dr. Scott Stouffer and Dr. Alejandro M. Briones for their numerical results and the probe. I also want to thank Hantae Kang for helping me throughout the project to run my experiments and being my research partner for the past year and a half.

Last but not the least I want to thank my family and friends who were encouraging and motivating during this project and providing me with emotional support.

TABLE OF CONTENTS

ABSTRACT	iii
ACKNOWLEDGEMENTS	v
LIST OF FIGURES	viii
LIST OF TABLES	xiii
LIST OF SYMBOLS	xiv
1 INTRODUCTION	1
1.1 Introduction	1
1.2 Importance of Experiments	2
1.3 Literature Review	5
1.3.1 Evolution of Micro Particle Image Diagnostic Techniques (μ PIDT's)	8
2 THEORY	13
2.1 Boundary Layer Theory	13
2.1.1 Falkner-Skan Theory	16
2.2 Particle Image Diagnostic Techniques (PIDT's)	17
2.2.1 Principles of PIDT's	17
2.2.2 Characteristics of PIDT's	22
2.2.3 Uncertainty in Velocity Calculations from PIDT's	25
2.3 PIDT'S Used for Boundary Layer Investigation	28
2.4 Illuminating the Flowfield	28
2.5 Light Source	32
2.6 Seed Material/Particles	33
2.6.1 Response Time	33
2.6.2 Dimensionless Parameters	34
2.7 PIDT Camera Optics	36
2.7.1 Focal Length	36
2.7.2 Magnification (M)	37
2.7.3 Field of View (FOV)	38
2.7.4 Depth of Field (DOF)	38
2.7.5 Working Distance (WD)	39
2.7.6 F-number ($f/\#$)	39

3	EXPERIMENTAL SETUP	42
3.1	Facility	42
3.2	Equipment for Experiments	43
3.2.1	High Speed Camera	43
3.2.2	Light Source	46
3.2.3	Pulse Generation	49
3.2.4	Particle Seeder	51
3.2.5	Computer and the Camera Software	52
3.3	Setup	53
3.3.1	Model Setup	53
3.3.2	Camera Setup and Focus	54
3.3.3	Light Source Setup	56
3.3.4	Target and FOV	57
3.3.5	Sequencing and Timing	57
4	RESULTS AND DISCUSSION	61
4.1	Theoretical Estimation of the Boundary Layer Thickness	61
4.2	Particle Image Diagnostic Techniques (PIDT's) Data Analysis	63
4.3	Particle Shadow Velocimetry (PSV)	66
4.4	Volume Illuminated Forward Scatter Particle Image Velocimetry (VIFS-PIV)	71
4.5	Particle Image Velocimetry (PIV)	75
4.6	Comparison Of The Three Experimental Techniques	77
4.7	Validation of the Numerical Investigation	80
5	CONCLUSION	85
6	RECOMMENDATIONS	87
	BIBLIOGRAPHY	88

LIST OF FIGURES

1.1	(a) Sampling probe used for experiments, (b) Cross section of the probe tip.[1]	1
1.2	Figure shows effect of Reynolds number on the flow around a cylinder (a) $Re = 1.54$, (b) $Re = 26$, (c) $Re = 140$, (d) $Re \approx 10^5$ and (e) $3 \times 10^5 < Re < 3 \times 10^6$. [2]	3
1.3	(a) Ludwig Prandtl with his flow visualization water tunnel, (b) Flow visualization in the replica of Ludwig Prandtl's channel. [5, 6]	4
1.4	(a) A small interrogation region showing Double Images in a Single Frame, (b) Correlation peaks obtained from a Double Image Single Frame using auto-correlation. [9, 10]	6
1.5	Composition of peaks in the cross-correlation function. [6]	7
1.6	Small interrogation regions taken from a pair of consecutive images using the Single Image Double Frame method.	7
1.7	Vector fields around a $30 \mu m$ obstacle showing the Hele-Shaw flow around the obstacle [14]. a) Instantaneous vector field measurement. b) Eight-image ensemble-averaged PIV velocity vector field.	10
1.8	Velocity data obtained from correlating a pair of PSV images at $M < 0.3$. [19]	11
1.9	Traces of particles 5 6 pixel long at $M = 0.7$. a) Cornstarch; b) $AlOx$; c) $TiOx$; d) Velocity vectors obtained from the traces correlation with displacements red green 45 pixel. [19]	12
2.1	Image shows a growing boundary layer over a flat plate and changing velocity gradient profile with position on the flat plate. [20]	13
2.2	Changing velocity gradient profile, Separation and back flow after separation. [20]	14

2.3	Image showing the freestream velocity, wedge half angle and the orientation of the axis.	16
2.4	(a) Light scattering from a 1 μm oil particle in air, (b) Light scattering from a 10 μm oil particle in air.[6]	20
2.5	(a) Inline illumination setup used in PSV, (b) Camera alignment shown for PIDT's capturing the scattered light.	22
2.6	(a) Low particle density image, (b) Medium particle density image, (c) Large particle density Image.[6]	25
2.7	Uncertainty in cross-correlated PIV data with varying particle image and interrogation size.[6]	26
2.8	: Measurement uncertainty as a function of displacement gradient for various particle image densities and interrogation window sizes.[6] . .	27
2.9	(a) Side view of the sheet forming optics in PIV, (b) Top view of the sheet forming optics in PIV.[6]	30
2.10	Schematic of the PSV illumination method.	31
2.11	Possible converging/diverging lens settings and recommendations. . .	31
2.12	(a) Top view of the volumetric illumination setting for VIFS-PIV, (b) Front view of the volumetric illumination setting for VIFS-PIV. . . .	32
2.13	An object placed at infinite distance is imaged at the focal point of the converging lens.	37
2.14	(a) Schematic of the large $f/\#$ and the speed of the camera, (b) Schematic of the small $f/\#$ and the speed of the camera.[28]	40
2.15	Plot showing the effect of $f/\#$ on DOF and the particle image diameter. 41	
3.1	(a) Shows the traditional mercury barometer and the thermometer with hygrometer, (b) Image shows the u-tube section of the manometer hooked up to the pitot static tube.	43

3.2	Image shows the screen shot of the Labview program with the inputs on the left under environmental parameters and the highlighted output as the required manometer reading.	44
3.3	Left to right, The pco.1600 camera and the control box from The Cooke Corporation.	45
3.4	Structural overview of the pco.1600 camera system.	46
3.5	Schematic of the laser head of Solo PIV.	48
3.6	(a) LED light source, (b) Quantum composer.	49
3.7	Architecture of the Pulse Generator.	50
3.8	to right, particle seeder control box and particle seeder.	51
3.9	(a) Three views of the smoke machine, (b) LeMaitre G300.	52
3.10	Top view of the experimental setup.	54
3.11	(a) Model placed close to the inlet of the test section using a bread board, (b) Model fixed to the metal post with the help of clamps. . .	55
3.12	Specially designed target, 14.0 mm wide and 10.5 mm high.	56
3.13	(a) Schematic showing the side view of the PIV experimental setup, (b) Schematic showing the top view of the PIV experimental setup. .	57
3.14	(a) Specially designed target, (b) Schematic showing the placement of the target.	58
3.15	Timing sequence in PSV technique.	59
3.16	Timing sequence in PSV technique.	60
4.1	Wedge half angle of the particulate sampling probe.	62
4.2	Theoretical velocity profile inside the boundary layer of the particulate probe.	63
4.3	Variation of the functions f and f'' with β	64

4.4	Raw image captured using the PSV technique showing the shadows of the probe tip and the particles on a bright background.	67
4.5	Velocity distribution obtained from processing a pair of PSV images seeded with talc shows biased velocity data due to the particle inertia and also shows two different brightness's from the two camera ADC's.	68
4.6	Velocity contour from PSV shows the averaged streamlines obtained from the biased velocity data resulting from the use of talc seed particles.	69
4.7	The relation between the size of the interrogation region, free stream velocity and the characteristic time.	70
4.8	(a): Averaged streamlines from 5 pairs of images with flow seeded with phenolic resin particles, (b) averaged streamlines from 4 pairs of images with flow seeded with glass balloons. Both images show a biased velocity data and curving of streamlines much later than they are expected.	71
4.9	Raw imaged captured using the VIFS-PIV technique.	72
4.10	(a) Velocity data obtained from a pair of images with a 32 pixel interrogation region, (b) Velocity data obtained from a pair of images with a 16 pixel interrogation region. These images show that in a 16 pixel interrogation region there are fewer number of detectable particles than the minimum number of particles required for the cross-correlation method.	73
4.11	A brighter image of Figure 4.7. Brightening the image shows the speckle noise in the image.	74
4.12	Velocity contour developed from the data obtained from VIFS-PIV shows streamline curvature as would be expected from a flowfield ahead of the probe.	74
4.13	Raw image obtained from the PIV technique with the strong reflection area highlighted.	75
4.14	Velocity data obtained from a pair of PIV images at 16 pixel resolution, a zoom in window shows the density of the velocity vectors.	76

4.15	Velocity contour and the streamlines obtained from averaging 27 pairs of images from PIV showing the streamline curvature as would be expected from a flowfield ahead of the probe and loss of data due to reflection from the probe surface.	77
4.16	Instantaneous images from (a) PSV, (b)VIFS-PIV and (c) PIV. . . .	78
4.17	Contour plot of the normalized velocity obtained from (a) PSV, (b) VIFS-PIV, and (c) PIV. Image shows the comparison between the velocity data obtained from the three PIDT's.	79
4.18	Images show an image of a uniform flow seeded with corn starch and the velocity data obtained from a pair of images.[19]	80
4.19	Non-dimensional velocity contour plots from (a) VIFS-PIV, (b) PIV and (c) Numerical investigation are shown. All plots are scaled from 0 ~ 1.4. In (c) a different velocity contour from the experiments is observed where the wedge half angle of the model changes.	81
4.20	Particulate sampling probe highlighting the bump closer to the tip of the probe.	82
4.21	Comparison of the non-dimensional velocity plot from the two variants of PIV and the numerical investigation taken 1.5mm ahead of the probe. 83	
4.22	Figure shows the percentage difference of the non-dimensional velocity obtained from one method with the other.	84
4.23	Comparison of the non-dimensional velocity plot from the two variants of PIV and the numerical investigation taken 1.5 mm parallel to the probe axis 0.5 mm away from the outer wall of the probe.	84

LIST OF TABLES

3.1	PSV light source specifications	47
3.2	Laser specifications	48
3.3	QC9614+ function modes	50

LIST OF SYMBOLS

A	Aperture/diameter of the lens aperture, m
a	Body radius, m
C, K	Constants
C_D	Coefficient of Drag
D	Probe diameter/characteristic length, m
D_D	Detectability criteria
d_i	Image distance, m
d_o	Object distance, m
d_p	Diameter of the particle, m
d_{scat}	Effective size/diameter of the scattered particle, m
$dt, \Delta t$	Small interval time, s
dt_{Q1}, dt_{Q2}	Q-switch time delay of first laser, s
$dx, \Delta x_x$	Small displacement, m
F	Focal length of lens, m
f, g, n	Similarity variables
$f/\#$	F-number
I	Intensity of light passing through the aperture
L	Length of the flat plate, m
M	Magnification of the Images
m	Wedge velocity component, m/s

Q_{eff}	Scattering efficiency
R	Correlation function
R_C	Convolution peak
R_D, R_{D+}, R_{D-}	Displacement peaks
R_F	Noise peak
Re	Reynolds number
Stk	Stokes number
t	Instantaneous time, s
U, V	Velocity of the fluid, m/s
u	x -component of velocity, m/s
V_p	Velocity of the particle, m/s
V_∞	Freestream velocity, m/s
v	y -component of velocity, m/s
x	x -coordinate of a point in space, length along the surface, m
Y, y	y -coordinate of a point in space, length perpendicular to the surface, m
β	Wedge half angle
γ	Kinematic viscosity of the fluid, m^2/s
δ	Boundary layer thickness, m
δ^*	Displacement thickness of the boundary layer, m
δ_z	Depth of field, m
θ	Momentum thickness of the boundary layer, m
λ	Wave-length of the light, m

μ_{∞}	Viscosity of fluid, Ns/m ²
ρ_p	Density of the particle, Kg/m ³
ρ_{∞}	Density of the fluid, Kg/m ³
τ_f	Characteristic time, s
τ_v	Response time, s
ϕ	Ratio of the instantaneous velocity to freestream velocity

Chapter 1

INTRODUCTION

1.1 Introduction

A numerical investigation was conducted on a particulate sampling probe (figure 1.1a) with conditions similar to a gas turbine at idle at the US Air Force Research Laboratories (AFRL) Propulsion Directorate. Numerical investigation on the probe included varying the dilution mass (figure 1.1b) that was added to the sample. Five different dilution percentages, 0, 60, 70, 90, and 95, were obtained in their numerical investigation. Experiments were conducted at University of Dayton Low Speed Wind Tunnel (UD-LSWT) on this probe to validate the numerical results. Experiments also focused on the study of the boundary layer growth on the probe and comparison of the experimental data with the analytical model.

The flow diagnostics were utilized in focused research. Particle Image Velocimetry (PIV), Particle Shadow Velocimetry (PSV) and Volume Illuminated Forward Scatter Particle Image Velocimetry (VIFS-PIV) were used for this study.

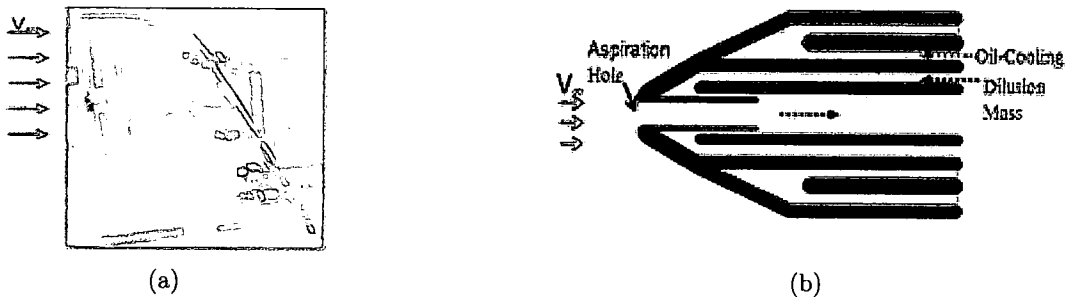


Figure 1.1: (a) Sampling probe used for experiments, (b) Cross section of the probe tip.[1]

1.2 Importance of Experiments

Solutions to most real world problems start with assumptions to simplify these problems. The real world constraints are imposed as the solutions to the simplified problems are better understood. Similarly for aerodynamic problems, assuming potential flow (incompressible, irrotational and inviscid) simplifies the problem and helps to determine a solution.

Assumption of potential flow has limitations. In flow around a cylinder; from a potential flow assumption we would expect no drag force acting on the cylinder, but a substantial amount of drag force can be measured acting on the cylinder. This condition is known as the d'Alembert's Paradox.

Figure 1.2 shows the flow past a cylinder. If potential flow is assumed, symmetrical streamlines can be seen symmetrical on both sides of the vertical plane of the cylinder. Figure 1.2a shows this symmetry with $Re = 1.34$. This falls under the regime of the Stokes Flow ($1 \leq Re \leq 4$ [2]). With increasing Reynolds number formation of vortices and then a separated flow at the back of the cylinder can be seen. This is caused by the viscous nature of the fluid.

The viscous nature of the fluid, say air or water can be ignored in cases where the flow has high Reynolds number. Reynolds number is given by:

$$Re = \frac{\rho_{\infty} V_{\infty} L}{\mu_{\infty}} \quad (1.1)$$

where, Re is the Reynolds number, ρ_{∞} , V_{∞} and μ_{∞} are the density, velocity and the viscosity of the freestream and L is the characteristic length of the flow. Instead for flows with low Reynolds number where either the freestream velocity is small or the

characteristic length is small the viscous effects on the solution of the flow become prominent.[3]

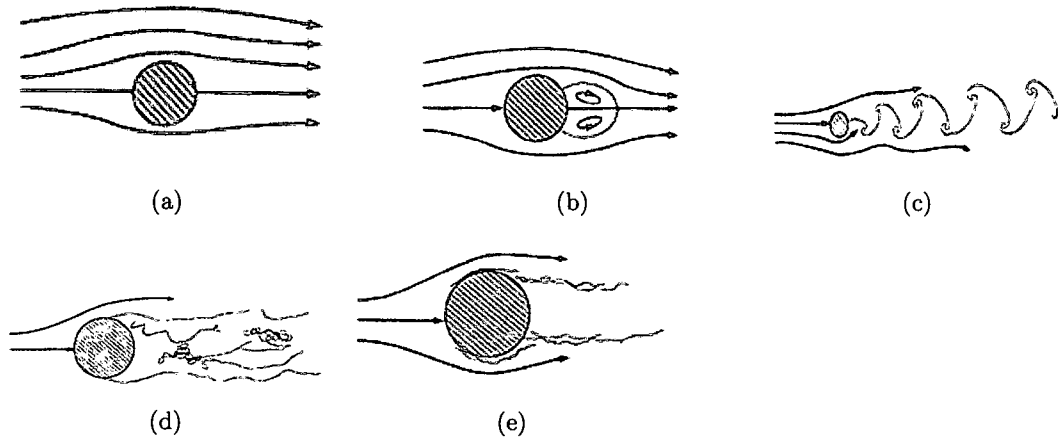


Figure 1.2: Figure shows effect of Reynolds number on the flow around a cylinder (a) $Re = 1.54$, (b) $Re = 26$, (c) $Re = 140$, (d) $Re \approx 10^5$ and (e) $3 \times 10^5 < Re < 3 \times 10^6$. [2]

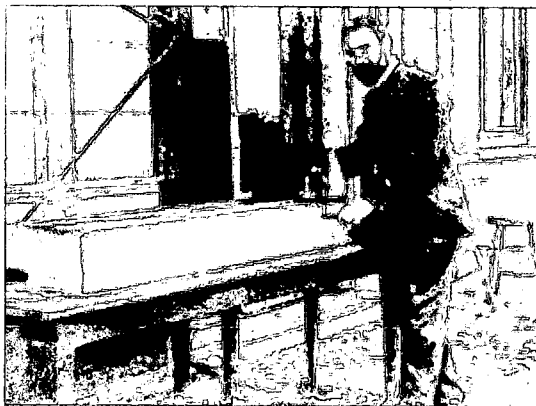
From the above examples it is evident that the viscous nature of the fluid can rarely be ignored completely. Any interaction of the flow with the model is influenced by the viscous nature of the flow and develops a boundary layer (thin layer over the surface of the model where the fluid velocity varies from zero velocity on the surface to the freestream velocity) on the surface of the model.

A model can be designed to be aerodynamically efficient if the interaction of the model with the surrounding flow is understood. Imagining or visualizing the flow past the model helps in understanding the interaction better. Leonardo Da Vinci was one of the earliest to have drawn very detailed visuals of the flow structure observations from behind the bodies in flowing water.[4] Early experiments on flow visualization were conducted by Ludwig Prandtl in early 1900. He performed the qualitative flow visualization experiments of unsteady flows behind the models in his water tunnel

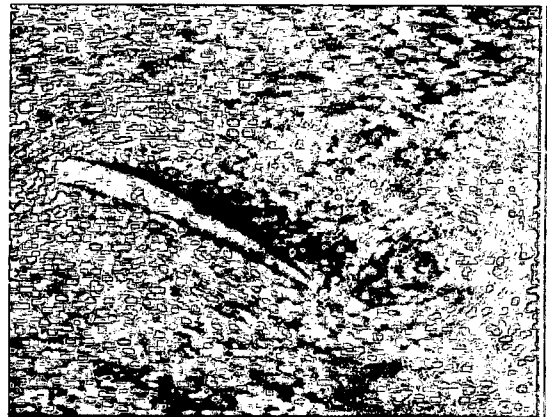
(Figure 1.3). Since Prandtl's experiment, a variety of flow visualization techniques have been developed and are both qualitative/quantitative in nature. Some examples

1. Qualitative flow visualization techniques are: Smoke Flow Visualization, dye flow visualization etc.
2. Quantitative flow visualization techniques or flow diagnostics techniques are: Particle Tracking Velocimetry (PTV), Particle Image Velocimetry (PIV) etc.

The qualitative flow visualization techniques allow an aerodynamicist to see the flow structures and help to interpret and understand the interaction between the flow and the immersed body. The quantitative flow visualization (Flow Diagnostic) techniques give quantitatively detailed information about the flowfield which helps in better understanding of the flow physics and quantifying forces due to fluid dynamic phenomena.



(a)



(b)

Figure 1.3: (a) Ludwig Prandtl with his flow visualization water tunnel, (b) Flow visualization in the replica of Ludwig Prandtl's channel.[5, 6]

A significant advancement in laser and digital camera technology and increasing computing speeds have widely increased the performance and abilities of flow diagnostic techniques. Since the early usage of laser scatter imaging for flowfield diagnostics in the 1970's, the flow diagnostic techniques have evolved accordingly. They are used to investigate flows across a range from simple flow uniformity to complex turbulence, from low Reynolds number subsonic flows to high Reynolds number sonic flows etc.

1.3 Literature Review

Turbulence in a flowfield was classically thought to be a stochastic process. In 1956 Townsend discovered the presence of coherent structures in turbulent flow using flow visualization.[7]

These historical examples prove the importance of accurate measurement techniques used to obtain a better understanding of the aerodynamics and a successful design. Aerodynamic data on a model can be measured using a variety of measuring techniques. Digital image processing of the flow visualization was a great leap forward over the measurement techniques called Quantitative Visualization Techniques.[7]

In early Particle Image Diagnostic Techniques (PIDT's) multiple images were taken and then distinct particles were tracked to extract the flowfield velocity data; this method is called Particle Tracking Velocimetry.

In PIDTs each image is divided into smaller regions and analyzed to extract the velocity data. In 1988 Adrian [8] demonstrated the statistical method to extract the velocity data from the images, also called the Optical Image Velocimetry (OIV). In his experiment each frame was exposed twice/multiple times (Figure 1.5a) in a short interval of time (the Double/Multiple Image Single Frame method) and then were

analyzed statistically (Figure 1.5b). This relation can be represented by:

$$R = R_P + R_{D-} + R_{D+} + (R_C + R_F) \quad (1.2)$$

where, R is the auto-correlation function, R_P is the self correlation peak (obtained due to the correlation of the particle image with itself), R_{D+} and R_{D-} are the displacement peaks obtained on opposite sides of R_P , and R_C and R_F are the noise peaks (peaks due to the convolution of the intensities and fluctuation of the noise component of the correlation estimator).

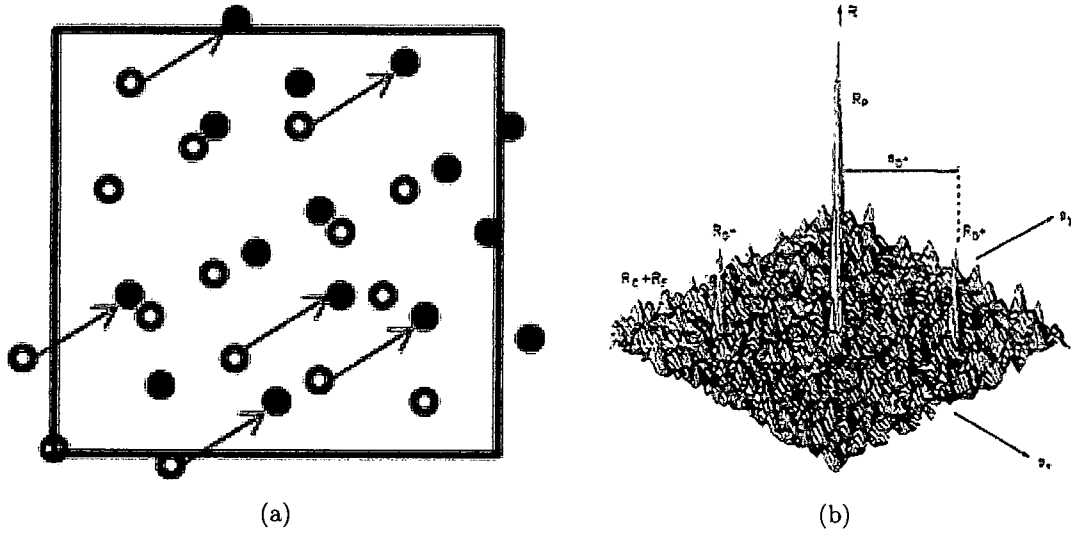


Figure 1.4: (a) A small interrogation region showing Double Images in a Single Frame, (b) Correlation peaks obtained from a Double Image Single Frame using auto-correlation.[9, 10]

In 1989 Cho [11] performed the statistical analysis on singly exposed PIV images to obtain the flowfield velocity data (Figure 1.5). Because each frame has a single image of each particle two consecutive images are taken for analysis (Figure 1.6). This

method is called Single Image Double Frame method or the Digital Image Velocimetry (DIV).

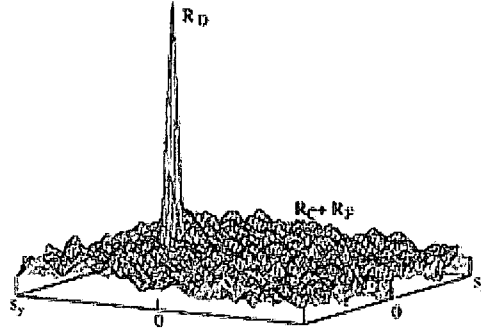


Figure 1.5: Composition of peaks in the cross-correlation function.[6]

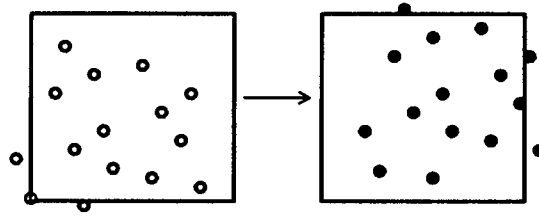


Figure 1.6: Small interrogation regions taken from a pair of consecutive images using the Single Image Double Frame method.

Keane et al [9, 10] talked about the parameters influencing the performance of PIV using the auto-correlation technique. In 1992 Keane et al [12] gave the parameters influencing the PIV using the cross-correlation technique. The most significant non-dimensional parameters identified in optimizing PIV performance when cross-correlation is used are:

1. data validation criterion such as the detectability criteria (DD) defined as the ratio of the first tallest peak to the second tallest peak

2. the particle image density
3. relative in-plane image displacement
4. the relative out of plane displacement
5. a velocity gradient parameter.

These parameters were investigated using the Monte Carlo method to validate their effect on the performance of PIV. The following were recommended for optimized PIV performance:

- 1: $D_D < 1.2$
2. at least 7 particles in each interrogation region
3. relative in-plane displacement should be less than 25% of the size of the interrogation region (on first iteration when using the multipass)[13]
4. out-of-plane displacement should be less than 25% of the thickness of the light sheet-velocity gradient factor less than 5%.

1.3.1 Evolution of Micro Particle Image Diagnostic Techniques (μ PIDT's)

Since the theory for PIDT's was laid out in the 1980's, these techniques have evolved with the evolving camera and computer technology and are improving the understanding of flow physics. In the 1990's focus was on developing high resolution PDIT's and their applicability.

In 1995 Keane et al [13] developed the Super-Resolution PIV (SRPIV). The SR-PIV algorithm has two parts: First analyzing the image with standard PIV correlation algorithms (auto-correlation) and second the Particle Tracking algorithm.

In 1998 Santiago et al [14] developed a PIV system for microfluidics with an interrogation volume spatial resolution of $6.9 \times 6.9 \times 1.5$ microns. The system used 100 - 300 nm diameter fluorescently tagged polystyrene particles with continuous Hg-arc lamp light source. Measurements were taken at a 3×10^4 Reynolds number in a Hele-Shaw flow field around a roughly circular obstruction with a $30 \mu\text{m}$ diameter (Figure 1.7). Using this PIV system, features including the stagnation points and high in-plane velocity gradients were observed.

In 1999 Meinhart et al [15] worked on development of microchannel flow measurements using PIV with a spatial resolution of $0.9 \mu\text{m}$. An Nd:YAG laser was used to illuminate the 200 nm fluorescent polystyrene particles. The experiments were conducted in a $30 \mu\text{m}$ high, $300 \mu\text{m}$ wide rectangular microchannel. Their PIV measurements were within 2% of various other micron-resolution velocimetry techniques.

Meinhart et al [16] demonstrated the Volume Illumination technique (illuminating the FOV with a volume of light instead of a thin sheet of light) for two-dimensional PIV. They observed that the Depth of Field (DOF) depends on the diffraction, geometrical optics and the particle size. They also noted that the volume illumination decreases the signal to noise ratio in the images which can be improved by (1) increasing the measurement depth, (2) decreasing the depth of the test section and (3) decreasing the particle concentration.

Olsen et al [17] addressed the issues relating to Volume Illuminated PIV and a new parameter, Particle Visibility (PV), was introduced. PV is dependent on the

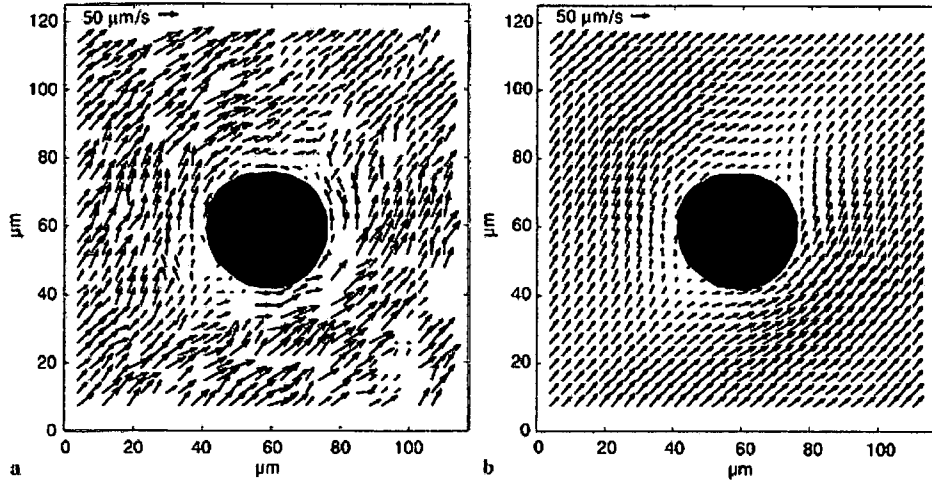


Figure 1.7: Vector fields around a $30\ \mu\text{m}$ obstacle showing the Hele-Shaw flow around the obstacle [14]. a) Instantaneous vector field measurement. b) Eight-image ensemble-averaged PIV velocity vector field.

focal number of the system, depth of the flowfield, diameter and concentration of the seed particles and is weakly dependent on the magnification.

Chetelat et al [18] performed miniature PIV with Light Emitting Diodes (LED's) as the light source. Three variants of illumination techniques, forward scatter, backward scatter and side scatter, were tested. Forward scatter illumination was found to be the most efficient among the three variants tested. Experiments were conducted in both water and air. Glass balls ($10\ \mu\text{m}$) were used as the seed particles in water, and spray droplets ($50\ \mu\text{m}$) or water fog ($20\ \mu\text{m}$) were used in air. Experiments were conducted with a field of view (FOV) of $6\ \text{mm} \times 5\ \text{mm}$ and objective $f/\#$ of 1.8. Results show that the forward scattered miniature PIV is a cheaper alternative than micro-PIV.

In 2005 Estevadeordal et al [19] demonstrated the use of Particle Shadow Velocimetry (PSV), shadows of the particles are imaged on a brighter background, for high-speed (Mach 0.7, transonic) flow applications. Tests were conducted in both air and water. Experiments were conducted to determine the performance of the method at low speeds, then at medium speed (Mach number < 0.3) and finally at transonic speeds.

At low speeds experiments in water were conducted with different seed material, bubbles and Polystyrene Latex (PSL) particles. With FOV's between 9 and 10 mm, exposure time was $50 \mu\text{s}$ when bubbles were used as seed material and $4 \mu\text{s}$ when PSL particles were used. In air experiments were conducted with smoke and also with cornstarch. A FOV of 3 mm was used to test the method with smoke and 10 mm for cornstarch. At Mach 0.3, tests were conducted in air with cornstarch and a FOV of 10 mm. Nicely correlated images were obtained at these speeds (Figure 1.8).

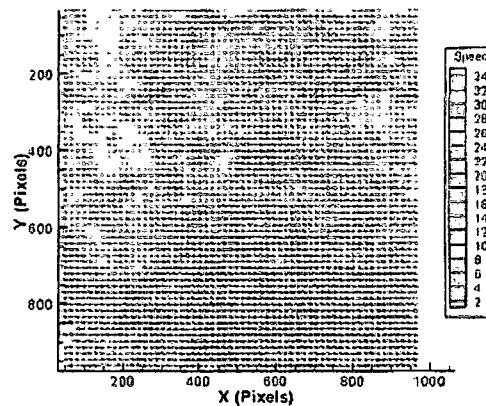


Figure 1.8: Velocity data obtained from correlating a pair of PSV images at $M < 0.3$. [19]

At 0.7 Mach, tests were conducted using cornstarch, AlO_x and TiO_x . At these speeds sparsely populated images were obtained. Traces of individual particles were observed and were used to correlate and find the velocity vectors (Figure 1.9).

Since the early PIV images in 1984, research was focused in developing the different PIDT's and their application to specific problems or their application with varying configurations. Since this study focuses on the comparative applicability of the three PIDT's, PSV, VIFS-PIV, and PIV, at high Reynolds number and small FOV, theoretical background on the PIDT's is important.

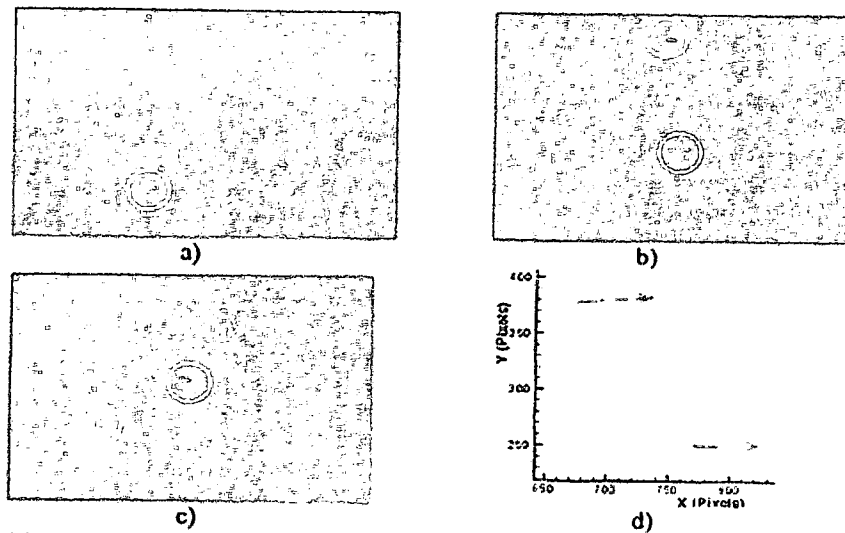


Figure 1.9: Traces of particles 5 6 pixel long at M 0.7. a) Cornstarch; b) AlO_x ; c) TiO_x ; d) Velocity vectors obtained from the traces correlation with displacements red green 45 pixel.[19]

Chapter 2

THEORY

2.1 Boundary Layer Theory

Boundary Layer Theory (BLT) was first introduced by Ludwig Prandtl in 1904. The viscous nature of the fluid flowing over a surface of the model causes the growth of the boundary layer on the surface of the model. The boundary layer (Figure 2.1) can be defined as the thin layer over the surface of the model where the fluid velocity varies from zero velocity on the surface to the freestream velocity.

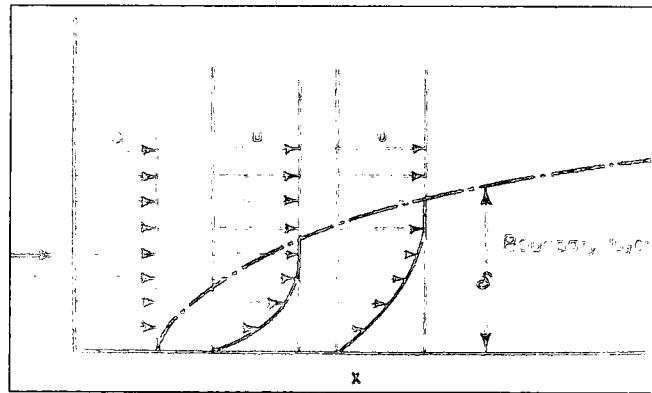


Figure 2.1: Image shows a growing boundary layer over a flat plate and changing velocity gradient profile with position on the flat plate.[20]

When a fluid moves against a pressure gradient over solid surface with a finite curvature, at some point on the surface, momentum and energy of the fluid in the boundary layer become insufficient to overcome the viscous force. The forward flow then separates and also creates a back flow (Figure 2.2).

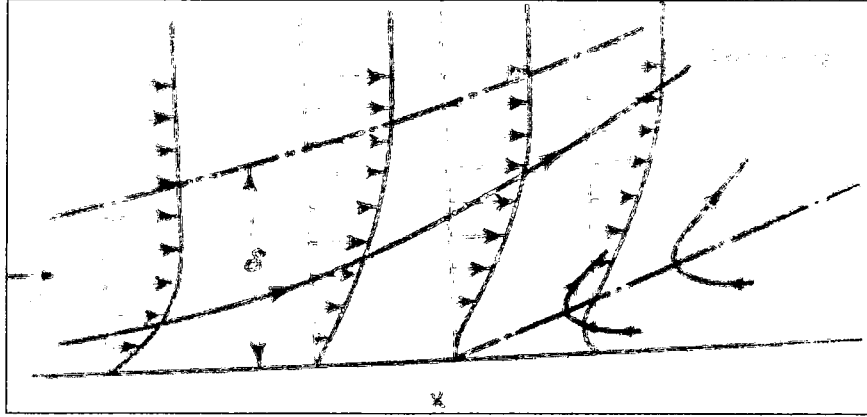


Figure 2.2: Changing velocity gradient profile, Separation and back flow after separation.[20]

For sufficiently large Reynolds numbers (Re) the influence of the viscosity of the fluid is confined to a thin layer close to the surface of the model. Consider the viscous flow over a flat plate with freestream velocity given by V_∞ , the residence time of the particle on the plate is L/V_∞ , where L is the length of the plate. Viscous effects spread across a streamline and are on the order of $\sqrt{\mu_\infty L / \rho_\infty V_\infty}$ [3], where μ_∞ and ρ_∞ are the viscosity and the density of the fluid. For high Re the diffusion time is much shorter than the residence time hence a thin boundary layer. If the $Re \gg 1$ then the thickness of the boundary layer is given by:

$$\delta \sim \frac{x}{\sqrt{Re}} \quad (2.1)$$

where, δ is the boundary layer thickness and x is the distance from the leading edge of the flat plate. This definition of the boundary layer thickness is obtained assuming:

1. $\delta \ll x$

2. normal velocity (v) \ll velocity parallel to the surface (u).
3. $u = V_\infty(y)$, where $V_\infty(y)$ is a second-order polynomial function
4. $\frac{\partial u}{\partial x} \ll \frac{\partial u}{\partial y}$
5. $\frac{\partial v}{\partial x} \ll \frac{\partial v}{\partial y}$

Thickness of boundary layer cannot be defined with definite values as the gradient in velocity increase asymptotically away from the solid boundary. The thickness of boundary layer can be defined in a couple of different ways [3]:

1. Displacement Thickness (δ^*)

Displacement thickness for the boundary layer is mathematically defined as:

$$\delta^* = \int_0^{Y \rightarrow \infty} \left(1 - \frac{U}{V_\infty}\right) \quad (2.2)$$

2. Momentum Thickness (θ)

Momentum thickness for the boundary layer is mathematically defined as:

$$\theta = \int_0^{Y \rightarrow \infty} \frac{U}{V_\infty} \left(1 - \frac{U}{V_\infty}\right) \quad (2.3)$$

where, Y is the coordinate perpendicular to the boundary surface, V_∞ is the freestream velocity and U is the local velocity.

2.1.1 Falkner-Skan Theory

In 1931 Falkner and Skan discovered boundary-layer similarity solutions for wedges. Considering the flow velocity is independent of the temperature and neglecting the buoyancy; the 2-dimensional continuity and momentum equations are given by:

$$\frac{\partial u}{\partial x} + \frac{\partial v}{\partial y} = 0 \quad (2.4)$$

$$u \frac{\partial u}{\partial x} + v \frac{\partial u}{\partial y} = U \frac{\partial U}{\partial x} + \gamma \frac{\partial^2 u}{\partial y^2} \quad (2.5)$$

where, U is the velocity of the flow at (x, y) , γ is the kinetic viscosity of the fluid u is the x-component of the velocity where x-axis is parallel to the wedge surface (Figure 2.3) and v is the y-component of the velocity and $u(x, y) = v(x, 0) = 0$, and $u(x, \infty) = U(x)$.



Figure 2.3: Image showing the freestream velocity, wedge half angle and the orientation of the axis.

Eliminating v from the momentum equation using the no-slip condition an integrodifferential equation is obtained. Combining the x and y variables into a single variable $\eta(x, y)$ and integrating gives:

$$f''' = f f'' \left(\frac{U g'}{\gamma g^3} \right) + (f'^2 - f f'' - 1) \left(\frac{\partial U}{\gamma g^2} \right) \quad (2.6)$$

where, $\frac{u}{U} = f'$ and $\eta = y g(x)$.

Falkner and Skan found that similarity was found when $\eta = Cyx^a$, which is consistent with power law freestream velocity given by:

$$U(x) = K^m \quad (2.7)$$

where, C is a constant such that η is non-dimensional and $C^2 = K(1+a)/\gamma$. Thus choosing,

$$\eta = y\sqrt{(a+1)\frac{U(x)}{\gamma x}} \quad (2.8)$$

Thus, substituting C value into g in Eq.3.6 gives the Falkner-Skan equation:

$$f''' + ff'' + \beta(1 - f'^2) = 0 \quad (2.9)$$

where, $\beta = (2a+1)/(a+3)$ and $\beta\pi/2$ is the wedge half angle (Figure 2.3).

Solution to the Falkner-Skan equation gives the values for f' which when substituted in Eq.s 2.2 and 2.3 give the displacement and the momentum thickness respectively. The Falkner-Skan solution of the boundary layer of a wedge is obtained assuming the flow is incompressible, Re is large, and the buoyancy force is negligible.

2.2 Particle Image Diagnostic Techniques (PIDT's)

2.2.1 Principles of PIDT's

The average velocity in terms of displacement and time is given by:

$$V = \frac{dx}{dt} \quad (2.10)$$

where, V is the average velocity, dx is the displacement and dt is the time taken for that displacement. If dt is infinitesimally small and tends to zero, then the velocity given by the above equation is the instantaneous velocity. PIDT's are based on this simple relation to find the flowfield velocity data.

In most PIDT's seed particles are introduced into the flow. This seeded flow is illuminated with a pulsed light source at short interval and the images of the seed particles in the flow are captured. The velocity of these particles is calculated using the known time interval and the displacements measured from the images using one of the statistical, auto-correlation method or the cross-correlation method. Images are captured either from the scattered light from the particles or the shadows cast by the particles.

Doubly or multiply (Figure 1.4a) exposed image frames in PIV are analyzed using auto-correlation method. The statistical relation of the auto-correlation function (Eq. 1.2) has five terms:

$$R = R_P + R_{D-} + R_{D+} + (R_C + R_F)$$

where, R is the auto-correlation function, R_P is the self correlation peak (obtained due to the correlation of the particle image with itself), R_{D-} and R_{D+} are the displacement peaks obtained on opposite sides of R_P , and R_C and R_F are the noise peaks (peaks due to the convolution of the intensities and fluctuation of the noise component of the correlation estimator).

R_{D-} and R_{D+} correlation components are obtained from correlation of the particles imaged in the first exposure with the identical particles imaged in the second

exposure and vice versa. This method of correlating the doubly exposed images results in the following disadvantages:

1. The two identical displacements peaks and result in an ambiguity in the displacement direction,
2. Zero displacement leads to the overlap of images and result in an overlap with the self-correlation peak.

In singly exposed image frames (Figure 1.5), two consecutive images short interval apart are statistically correlated using the cross-correlation method. The statistical cross-correlation function has three components:

$$R = R_P + R_D + (R_C + R_F) \quad (2.11)$$

where, R_D is the displacement peak, and R_C and R_F are the noise peaks.

In a cross-correlation method each particle image in the first frame is correlated with the particle images only in the second frame. This method of correlating the PIV images results in the following advantages:

1. When single exposure images are superimposed after digitization, it shows a lower noise level compared to the auto-correlation method
2. This method has solved the problem of ambiguity over the direction of the extracted velocity data
3. This method is computationally less intensive

Images Captured from the Scattered Light of the Particles

Quantitative Flow Visualization/PIDT's give extensively detailed information about the flowfield and a way to understand the interaction of the flow with the model. PIDT's have their roots in Laser Speckle Velocimetry (LSV). In early Particle Image Velocimetry (PIV), a well known PIDT, images were considered the speckle images until 1984 when it was argued that the concentration of seed was not enough to make the speckle pattern.[21]

PIV is based on the scattering of light from a seed particle in the flowfield. The size of the particles used in PIV are in the range of the wavelength of the light used or bigger. The light scattering from the seed particles can be explained using Mie scattering theory.

Figure 2.4 shows the light scattering from an oil particle on a logarithmic scale. Comparing Figure 2.4a and Figure 2.4b it is clear that the larger particles have a higher ratio of the intensity for forward and backward scatter. Figure 2.4 also indicates that the use of forward scatter produces brighter images, but the thin sheet of illumination in PIV imaging prefers a 90° angle.

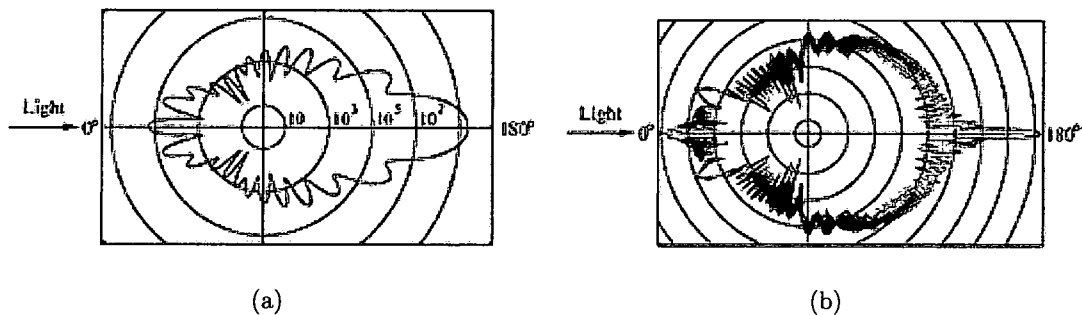


Figure 2.4: (a) Light scattering from a 1 μm oil particle in air, (b) Light scattering from a 10 μm oil particle in air.[6]

The scattering efficiency in Mie scattering is defined as [22]:

$$Q_{eff} = \frac{4d_{scat}}{\pi d_p^2} \quad (2.12)$$

where, Q_{eff} is the scattering efficiency, d_{scat} is the effective size of the scattered particle and d_p is the diameter of the particle. d_{scat} for a particle is a function of the refractive index of the particle, diameter of the particle and the wavelength of the light.

From Figure 2.4 it is evident that light is being scattered from all angles. This means a large number of particles show the multi scatter phenomenon when in the illuminated flowfield. Effectively it means that the intensity of the image increases with the presence of large particles and also with a high density of particles in the flowfield. This phenomenon has two associated disadvantages (1) it increases the noise level in the images and (2) it increases the influence of large particles on the PIV result which makes it harder to estimate the size of the particles in the image and the corresponding velocity lag.

Images Captured from the Shadow of the Particles

Particle Shadow Velocimetry (PSV) captures the images of the particles by capturing the shadow (light extinction) of the particles on a bright background in contrast to the images captured from PIV, where scattered light forms a bright particle on a dark background. Casting particle shadows in the images are the consequence of the inline illumination (Figure 2.5a) of the flowfield with a low energy incoherent light in PSV. In PSV particles lie between the light source and the camera, the shadow cast

by the particle is imaged on the camera sensor which is an inverse image compared to the image captured by PIV.

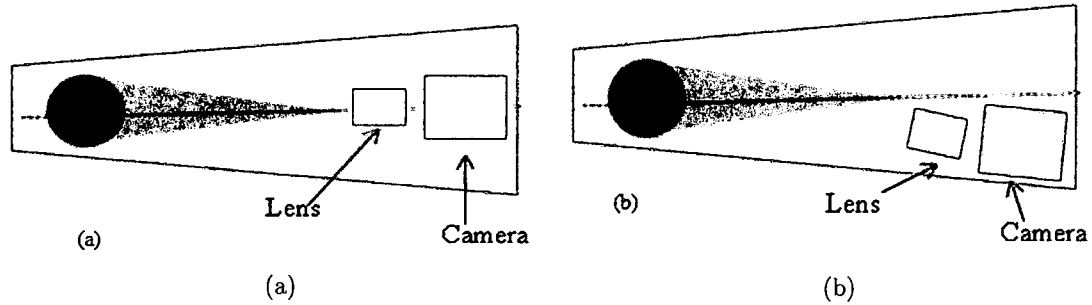


Figure 2.5: (a) Inline illumination setup used in PSV, (b) Camera alignment shown for PIDT's capturing the scattered light.

Chetelat et al [18] found that PIV with LED's was most efficient in the forward scatter illumination variant. The ratio of extinction of light in PSV with forward scatter depends on the size of the particle; but in most cases, extinction is ten times larger [19] causing no deterioration in the ability to obtain good cross correlation from the images.

2.2.2 Characteristics of PIDT's

General Characteristics of PIDT's are as follows:[6]

1. **Non-intrusive:** PIDT's do not employ any physical probe in the flowfield like the other diagnostic techniques, pressure probes or hotwire probes, for flowfield diagnostics. PIDT's are optical techniques and are therefore nonintrusive in nature and can be applicable to any speed range.
2. **Indirect:** Like the hotwire probes or the pressure probes PIDT's do not measure the velocity of the fluid particles, they measure the velocity of the seed

particle introduced in the flow and are therefore they are called indirect flow measurement techniques except in multi phase flows.

3. **Whole field:** PIDT's capture the large images of the flowfield and extract velocity information out of these images. This is unique to PIDT's, whereas the other flow diagnostic techniques obtain the data at a point.
4. **Velocity lag:** To be able to measure the flow velocity accurately the seed particles have to follow the flow faithfully this means that the size of the particles have to be small and have similar density or else they tend to move slower and also have the effect of gravity on their motion.
5. **Illumination:** The illuminating light source depends on the type of the particle imaging technique employed. For the Particle Image Velocimetry (PIV) the light source should generate high power light (such as coherent lasers) whereas for the Particle Shadow Velocimetry (PSV) we need low power light source preferably incoherent.
6. **Duration of illumination pulse:** The illumination pulse must be short enough to capture the frozen image of the particles and not image streaks.
7. **Time delay between illumination pulses:** The Time delay between two consecutive pulses should be long enough to be able to capture the range of the velocities and see the movement of the particles but should also be short enough so that the particle would not depart the interrogation region. Similarly if the flow has any out of plane velocity then the particles should be captured before they are out of the plane of measurement.

8. **Distribution of seed particles:** In flow visualization techniques, smoke flow visualization or dye flow visualization, only certain areas are marked with the seed particle whereas in the PIDT's a homogenous distribution of medium density is desired.
9. **Density of images of seed particles on images:** Particle Densities can be separated into three different categories (Fig. 2.6). Figure 2.6a shows a low particle density image. In low particle density images individual particles can be traced in image pairs and the method is called Particle Tracking Velocimetry (PTV). Figure 2.6b shows a medium density particle image in which we can see individual particle but it is hard to track the individual particle in the image pair and needs statistical methods to correlate images. Figure 2.6c shows a high density image in which it is hard to distinguish between individual particles. This method is called Speckle Velocimetry.
10. **Number of illuminations per recording:** It is possible to take more than one image on a single frame and obtain the velocity data (auto correlation). The method of taking a single image on a single frame to obtain the velocity data from two separate frames is called cross correlation.
11. **Size of the interrogation region:** The size of the interrogation region is a measure of the spatial resolution of the velocity data; the smaller the size the higher the resolution. The size of the interrogation region should be small enough so that it does not have any influence from the resulting velocity gradients.

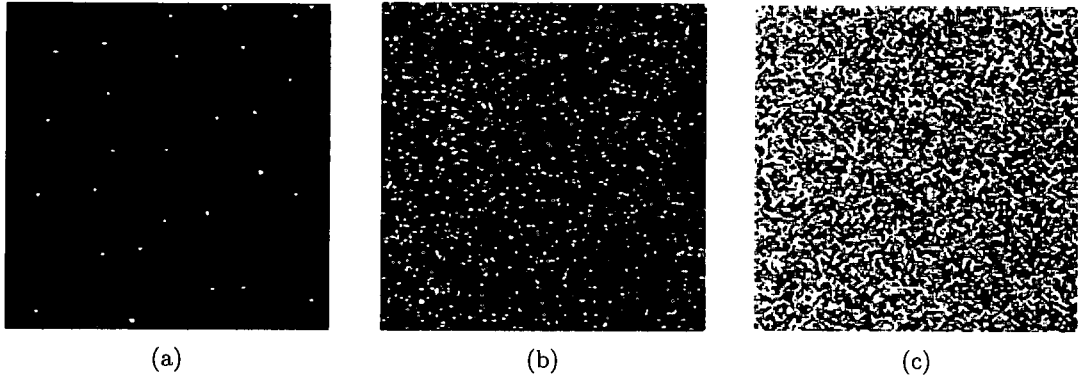


Figure 2.6: (a) Low particle density image, (b) Medium particle density image, (c) Large particle density Image.[6]

2.2.3 Uncertainty in Velocity Calculations from PIDT's

The velocity from PIDT images is computed using:

$$U = \frac{\Delta x}{\Delta t \cdot M} \quad (2.13)$$

where, Δx is the average displacement of the particles in the image, Δt is the time interval between the two light pulses, and M is the magnification of the captured images. The displacement in pixels is obtained by using peak locator algorithms (e.g. a centroid method) that find the location of the peak on the correlation map obtained from cross-correlating the two images and corrects for various biases and yields to sub-pixel accuracy (< 0.1 pixels).[6, 7, 23]

Figure 2.7 shows the uncertainty in the cross-correlated PIV data of a uniform flowfield with displacement calculated using Monte Carlo method. Three different cases are shown with different particle image and interrogation size. From Figure 2.7 it can be observed that increasing the particle image size (dz) increases uncertainty

in the data. If $dz < 1$ pixel, a phenomenon called 'pixel locking occur'. The optimal value of $dz \sim 2$ pixel. Increasing the size of the interrogation region decreases the uncertainty in the data as the increase in the size of the interrogation increases the number of detectable image pairs contributing to the correlation peak.

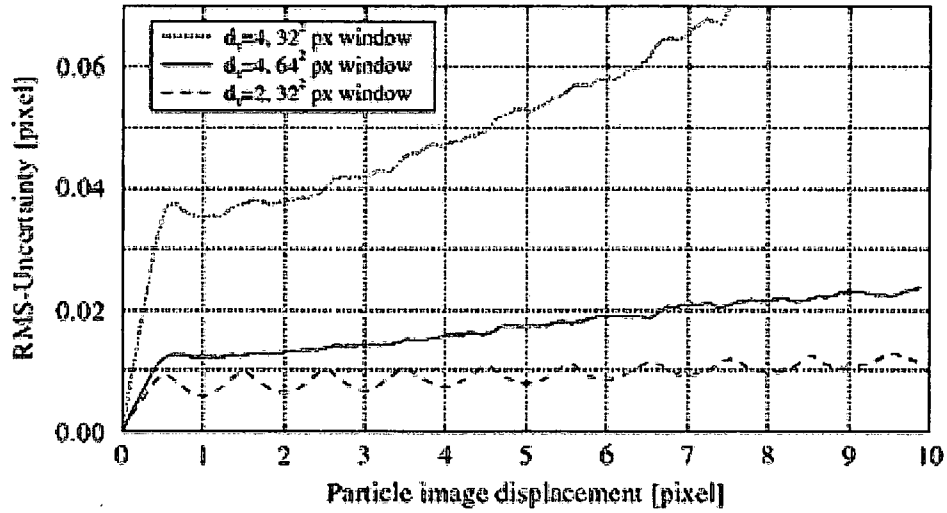


Figure 2.7: Uncertainty in cross-correlated PIV data with varying particle image and interrogation size.[6]

In a gradient flow uncertainty in regions with lower velocities is higher. Figure 2.8 shows the uncertainty as a function of displacement gradient for various interrogation region sizes and the particle densities of the interrogation region. It is evident that larger interrogation regions are associated with larger uncertainty as the gradient across a larger area is higher and the velocity is biased towards the lower velocities in the interrogation region. Lower density interrogation regions give a smaller correlation peak which leads to a higher uncertainty compared to higher image density interrogation region.

Analyzed PIV data is averaged to eliminate fluctuations due to turbulence in the flow. The velocity averaging routines allow removal of outliers beyond any number of standard deviations along with other filtering techniques. Typically averaged data is presented using the median to clearly show various flow patterns for each configuration. The median is less affected by "outliers" than the mean and offers a smooth representation of the ensemble-average velocity fields.

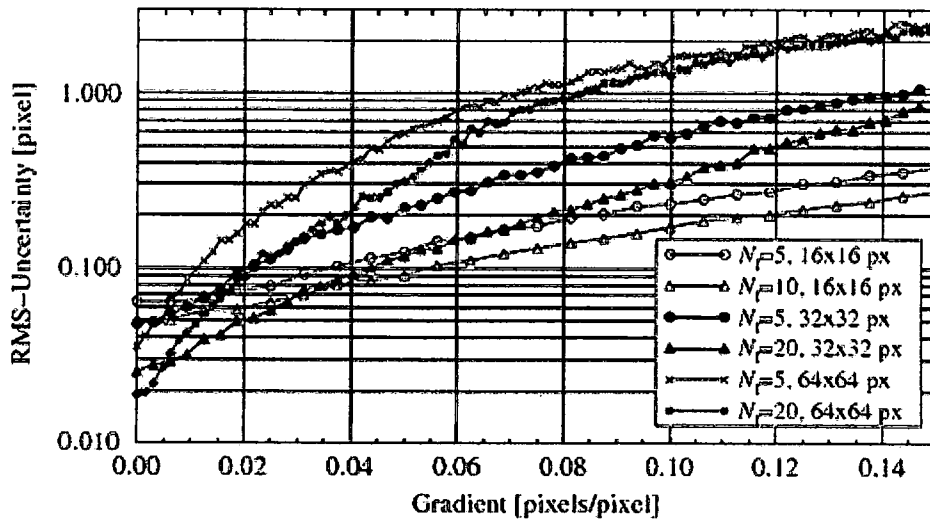


Figure 2.8: : Measurement uncertainty as a function of displacement gradient for various particle image densities and interrogation window sizes.[6]

Various routines/filters have been developed to reduce the uncertainties in the PIV data. Each has a unique implementation in reducing the error in the data. The multi-step or the iteration analysis of the PIV data can be performed in two ways:

1. Multi-grid analysis where the interrogation size is decreasing progressively with every iteration. In this method the criterion for inplane movement can be neglected for the smallest interrogation regions.

2. Keeping the size of the interrogation region constant in all iterations which enhances the image resolution.

A multi-pass routine uses a window shift technique to improve the correlation. Shifting the second interrogation window by a discrete amount (mean velocity) will lead to a correlation of more image pairs. This results in a higher correlation peaks (better signal to noise ratio). A priori knowledge of the flowfield is required to implement the window shift technique on the first iteration, but on the second or higher iteration information from previous iterations can be utilized.

Spatial resolution can be increased effectively with a higher spatial sample rate. This can be achieved with a 75% overlap between the neighboring interrogation regions.

2.3 PIDT'S Used for Boundary Layer Investigation

Three different PIDT's, Particle Image Velocimetry (PIV), Particle Shadow Velocimetry (PSV) and Volume Illuminated Forward Scatter Particle Image Velocimetry (VIFS-PIV), are selected to study the boundary layer on the sampling probe. Details of each method are given below.

2.4 Illuminating the Flowfield

Though the working principle behind PIV, PSV and VIFS-PIV is similar, the basic difference between PIV and the other two methods is the illumination of the plane of focus. In PIV sheet forming optics are used to precisely form a thin sheet in

the plane of interest (~ 0.5 mm), whereas the PSV and VIFS-PIV techniques use the volume illumination method.

PIV is a well known and accepted flow diagnostic technique. PIV uses a high energy coherent light to form a thin sheet of light in the focus plane to illuminate the particle in that plane and image the light scattered from these particles. This thin sheet of light is formed using the appropriate optics. The configuration of the optics (Figure 2.9) used to form the light sheet is called Sheet Forming Optics (SFO)/Light Sheet Optics (LSO).

The PIV system uses the Solid State Neodymium doped Yttrium-Aluminum-Garnet (Nd:YAG) laser as the light source. Nd:YAG lasers are a high power coherent light source and therefore the sheet forming light source in PIV needs three lenses (Figure 2.9), (1) diverging lens (2) lens to generate the light sheet of constant height and (3) lens focus the light to the appropriate thickness. Lens 2 is used for generating the light sheet of constant height. It is optional in many cases where the height of the sheet required is big and cannot be generated using a lens.

Figure 2.9 shows three lenses as required by PIV to form a constant height laser sheet. A double concave lens (first lens) with -50 mm focal length is the diverging lens in the SFO, a convexo-planar (second lens) lens with a 200 mm focal length is the lens used to generate the sheet of constant height and the double convex lens (third lens) is the lens used for controlling the thickness of the light sheet.

PSV uses an incoherent low power light source. This allows for a direct inline illumination of the camera. The system of illumination in PSV technique needs no sheet forming optics. An example of the inherent nature of the light disperses and

illuminates the flowfield volume. A schematic for inline volume illumination for PSV can be seen in Figure 2.10.

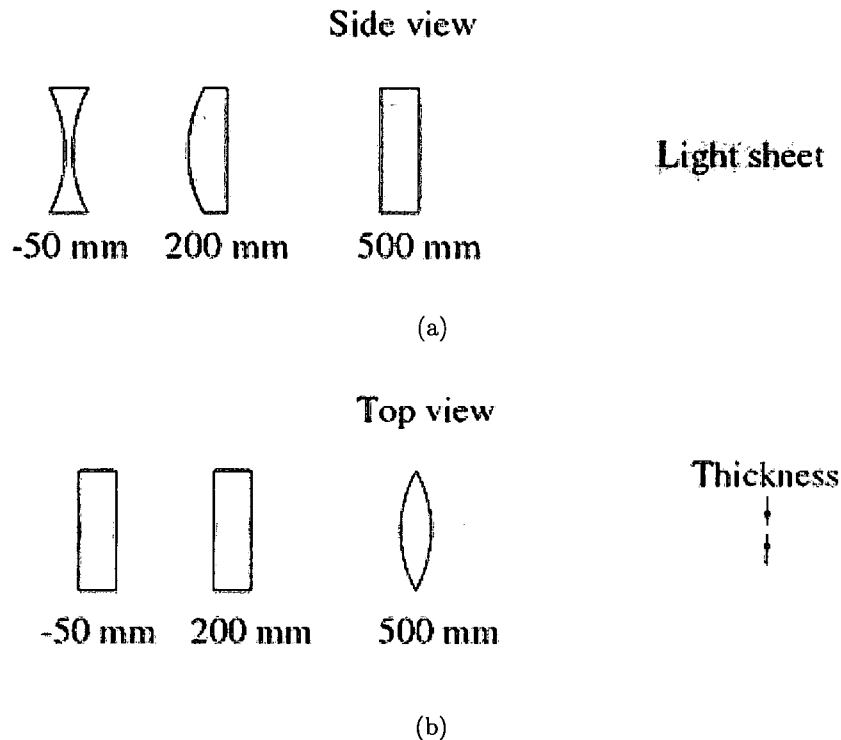


Figure 2.9: (a) Side view of the sheet forming optics in PIV, (b) Top view of the sheet forming optics in PIV.[6]

The light source used in the VIFS-PIV technique is an Nd-YAG laser. The coherent nature and high power of the laser light makes it difficult for inline illumination without causing damage to the camera sensor. Sheet forming optics are used for volume illumination in VIFS-PIV. A diverging (Figure 2.11a and c) lens is used to disperse the coherent laser beam. Figure 2.11 shows the possible settings and recommendations of the converging/diverging lens for sheet formation. Any setting where secondary reflections from the lens surface retrace the path is not recommended. This

dispersed light is then used to illuminate the flowfield at an angle so that the light beam does not hit the camera.

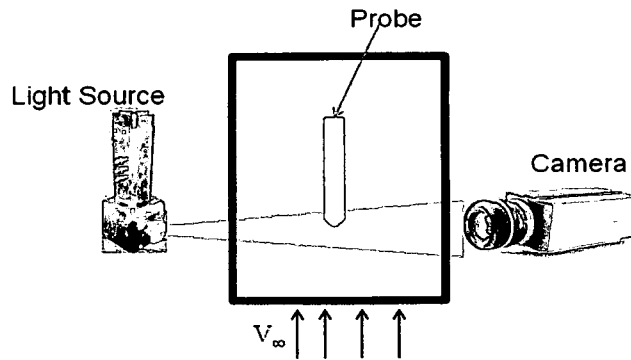


Figure 2.10: Schematic of the PSV illumination method.

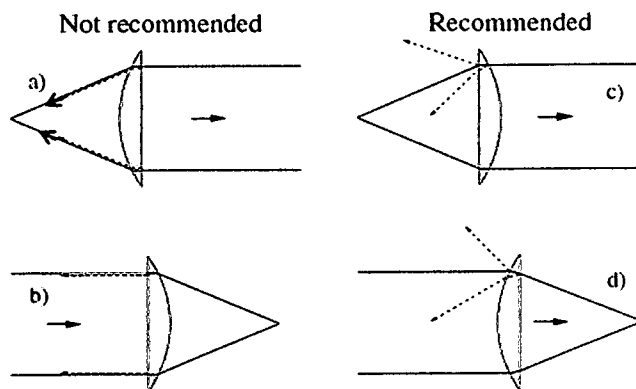


Figure 2.11: Possible converging/diverging lens settings and recommendations.

In Figure 2.12, the top view and the front view of the volume illuminating optics setup for VIFS-PIV are shown. Care should also be taken while illuminating the flowfield in VIFS-PIV. Large reflections on the camera sensor from any surface can damage the camera sensor permanently. Once the optics are set and the path of

the laser is known, the laser power should be increased slowly while simultaneously checking for any possible saturation on the camera sensor due to reflections thus ensuring the safety of the camera so that there are no large reflections.

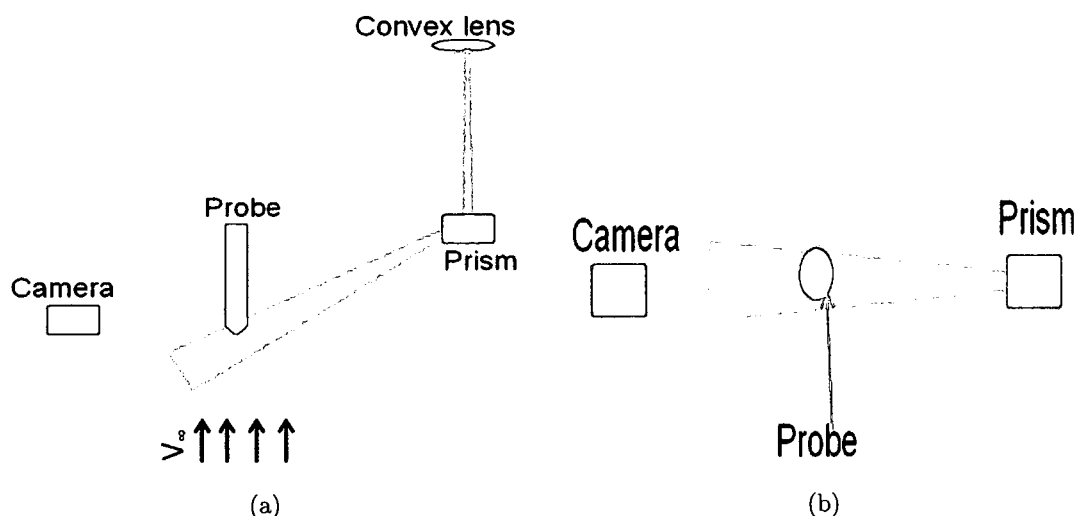


Figure 2.12: (a) Top view of the volumetric illumination setting for VIFS-PIV, (b) Front view of the volumetric illumination setting for VIFS-PIV.

2.5 Light Source

PIV and VIFS-PIV use the high energy pulsed coherent light source. Particles in both techniques are imaged from the scattered light from. In PSV an incoherent low power light source is used and the shadows of the particles are imaged. Further details of the light source are discussed in the Chapter III.

2.6 Seed Material/Particles

PIDT's, as discussed, are indirect measurement techniques; therefore it is important to understand the fluid mechanical properties of the seed material used in these PIDT's.

2.6.1 Response Time

All experiments are influenced by some associated error factors. One error in flow diagnostic techniques is caused due to the buoyancy force acting on the particles. The difference in the density of the particle and the fluid and the size of the particle cause the difference in motion between the particle and the fluid. The equation of motion of the particle in the fluid is given by:[24]

$$\frac{dV_p}{dt} = \frac{18\mu_\infty}{(\rho_p - \rho_f)d_p^2} \frac{C_D Re}{24} (V_\infty - V_p) \quad (2.14)$$

where, μ_∞ is the freestream viscosity of the fluid

Re is the Reynolds number

ρ_p, ρ_f are the density of the particle and the fluid respectively

d_p is the diameter of the particle

C_D is the coefficient of drag

t is the instantaneous time

V_∞ is the freestream velocity

V_p is the velocity of the particle.

Assuming the Reynolds number is small, the equation of motion can be simplified to:[6, 24]

$$V_p = V_\infty (1 - \exp(t/\tau_v)) \quad (2.15)$$

where, τ_v is the response time of the particle.

The response time of the particle suspended in a fluid is defined as the time required by the particle to achieve 63% freestream velocity from rest.[24] The response time of a particle in the fluid is given by:[6]

$$\tau_v = d_p^2 \frac{\rho_p}{18\mu_\infty} \quad (2.16)$$

Typical response times for talc and smoke were around 1 to 12 msec and 4 μ sec respectively.

2.6.2 Dimensionless Parameters

Dimensionless/non-dimensional parameters are the quantities with partial or full units removed. They can be defined as scaling of the variables by a reference value.

Non-dimensionlizing the quantities give the following advantages:

1. It reduces the number of quantities influencing the equation/problem.
2. It allows the comparison of the analysis regardless of the units and the system of units in which the analysis is done.
3. It allows the estimation of the effect of each parameter and its magnitude on the equation.

The Stokes number is one dimensionless parameter of interest to the studies performed here. It gives an estimate of the influence of the physical characteristics of the seed material on the behavior of the seed particles in the flow diagnostic application.

Stokes Number

Stokes number is defined as the ratio of the inertia force of the particle to the Stokes resistance acting on the particle due to the viscous nature of the fluid.[25] The Stokes number for a particle in a moving fluid can be calculated using:[24]

$$Stk = \frac{\tau_v}{\tau_f} \quad (2.17)$$

where, τ_f is the characteristic time given by:

$$\tau_f = \frac{D}{V_\infty} \quad (2.18)$$

where, V_∞ is the freestream velocity and D is the characteristic length. Substituting the response time and the characteristic time in Eq. 2.17 gives:

$$Stk = \frac{\rho_p d_p^2 V_\infty}{18\mu_\infty D} \quad (2.19)$$

Stokes number is a good estimate of the motion of the particle in the fluid. If $Stk \ll 1$ and the particle's response time is much less than the characteristic time which means the particle follows the flow faithfully and the particles are called the Stokesian particles [26], on the other hand if $Stk \gg 1$ then the particles do not follow the fluid flow faithfully.

This relation can further be explained using the velocity ratio $\phi = U/V_\infty$ where, U is the velocity of the particle. The velocity ratio in terms of Stokes number is given by:[24]

$$\phi = \frac{1}{1 + Stk} \quad (2.20)$$

This relation between the Stokes number and velocity ratio explains the constraint on the Stokes number. $Stk \ll 1$ implies that $\phi \sim 1$, which means the velocity of the particle is equal to the velocity of the freestream and follows the flow faithfully. In contrast, if $Stk \gg 1$ this implies $\phi \ll 1$ and the particles do not follow the flow faithfully.

2.7 PIDT Camera Optics

Understanding the camera optics is also very important in order to be able to take the desired images for flow diagnostics. The following is a brief discussion of the influence of different camera parameters on the captured images.

2.7.1 Focal Length

When an the object is placed at infinite distance from the lens then the distance from the middle of the lens to the image plane (focal plane) is called the focal length of the lens. Figure 2.13 shows the image of an object focused using a double convex lens. The focal length of a lens is measured by:

$$\frac{1}{d_o} + \frac{1}{d_i} = \frac{1}{f} \quad (2.21)$$

where, F is the focal length of the lens, d_i is the distance along the axis of the lens from the center of the lens to the image plane (image distance), d_o is the distance from the center of the lens to the object along the axis of the lens (object distance). The focal length of the lens influences the depth of field of the images (discussed in detail in later sections).

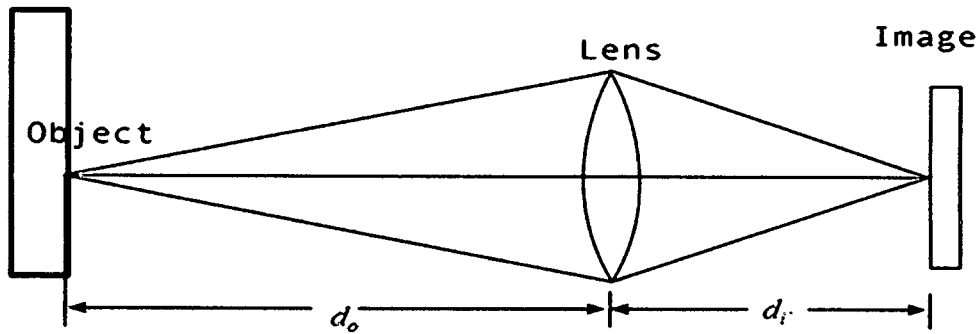


Figure 2.13: An object placed at infinite distance is imaged at the focal point of the converging lens.

2.7.2 Magnification (M)

The magnification of a lens is defined as the ratio of the image size over the object size or the image distance over the object distance. The relation between the magnification and the depth of field is defined in later sections. Magnification of an image is mathematically given by:

$$M = \frac{d_i}{d_o} \quad (2.22)$$

2.7.3 Field of View (FOV)

Field of View (FOV) is defined as the visible area in the plane of focus of the camera. The size of the FOV is directly proportional to the magnification of the lens. For a given image distance and object distance the size of the FOV is indirectly proportional to the focal length of the lens.

2.7.4 Depth of Field (DOF)

Assume an object is at a finite distance from the lens and focused on the focal plane. Moving the object either closer or further from the lens decreases the sharpness of the image gradually, thus the total distance where the loss the sharpness of the image is imperceptible to normal vision is called Depth of Field (δ_z).

The depth of field influences the data quality of the experiments using PIDT's. A thick DOF for the experiment means, particles out of the plane of interest also influence the velocity data obtained from the experiments i.e. noise in the data also contribute to the results. Therefore, a thin Depth of field is desired.

Depth of field for a setup is a function of the working distance, focal length and the aperture of the camera. The relation between the DOF, working distance (WD), the focal length (F) and the aperture (A) is given by:[4]

$$\delta_z = 4(1 + M^{-1}) \left(\frac{F}{A} \right)^2 \lambda \quad (2.23)$$

where, λ is the wavelenght of the light.

2.7.5 Working Distance (WD)

The working distance is defined as the distance between the lens and the object plane (plane of focus). The WD for a particular setup depends on the focal length of the lens used on the camera and any spacers used between the camera and the lens.

For a given magnification and aperture of the lens, the WD is proportional to the focal length of the lens.

Figure 2.13 shows the influence of the WD on the DOF. A smaller WD results in smaller DOF. For a given aperture (A), is the diameter of the camera opening) and the WD, the DOF is mathematically defined as:[27]

$$\delta_z = (WD)^2 \left(\frac{1}{1000A + WD} + \frac{1}{1000A - WD} \right) \quad (2.24)$$

2.7.6 F-number ($f/\#$)

The quality of the images is an important factor for optimal flow diagnostics. The quality of the captured images is defined by the spatial resolution and the noise level in the images. Noise levels in images increase with the increasing DOF which is a function of the diameter of the camera aperture. Thus the quality of the captured images depends on the aperture of the camera through which light is allowed to pass and hit the camera sensor. The size of the aperture of the camera lens is measured in terms of F number ($f/\#$). F number is a dimensionless number that is a quantitative measure of the lens speed. A lens with a larger aperture is called a fast or high speed lens.[28] Figure 2.14 shows the comparison of the $f/\#$ and the speed of the camera.

Mathematically $f/\#$ is defined as:

$$f/\# = \frac{f}{A} \quad (2.25)$$

where, f is the focal length of the lens and A is the diameter of the aperture.

Decreasing $f/\#$ means an increase in the aperture diameter and vice versa (Figure 2.14) i.e., $f/\#$ is also a measure of the amount of light passing onto the camera sensor. The amount of light passing through the aperture of the camera is inversely proportional to the square of the $f/\#$. A decrease in $f/\#$ by half increases the amount of light passing through the aperture by four times.

$$I \propto \frac{1}{(f/\#)^2} \quad (2.26)$$

where, I is the intensity of the light passing through the camera aperture.

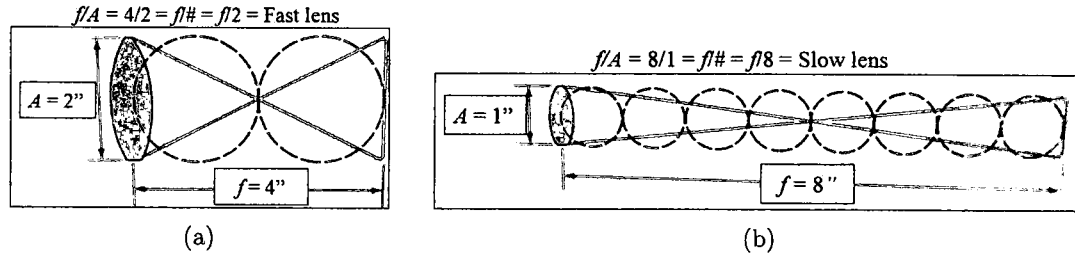


Figure 2.14: (a) Schematic of the large $f/\#$ and the speed of the camera, (b) Schematic of the small $f/\#$ and the speed of the camera.[28]

F-number of the camera also determines the DOF (δ_z) of the captured images. Large amounts of diffracted light reach the sensor at smaller $f/\#$ which results in a thin DOF. Figure 2.15 shows the theoretical results of the effect of the $f/\#$ on the image diameter (d_i) and the DOF for a given magnification of $1/4$ and a 1 micron

particle diameter (d_p). Image diameter and DOF increase with increasing $f/\#$. An increasing particle image diameter or DOF increases the uncertainty in the PIV data (Figure 2.7). There is an optimal particle image diameter ~ 2 pixels.

This chapter presented the theoretical background needed for the study of the comparison of application of the selected PIDT's to a high Re flow with small FOV. In the following chapter, all the experimental equipment used are listed with the detailed explanation of the experimental setup.

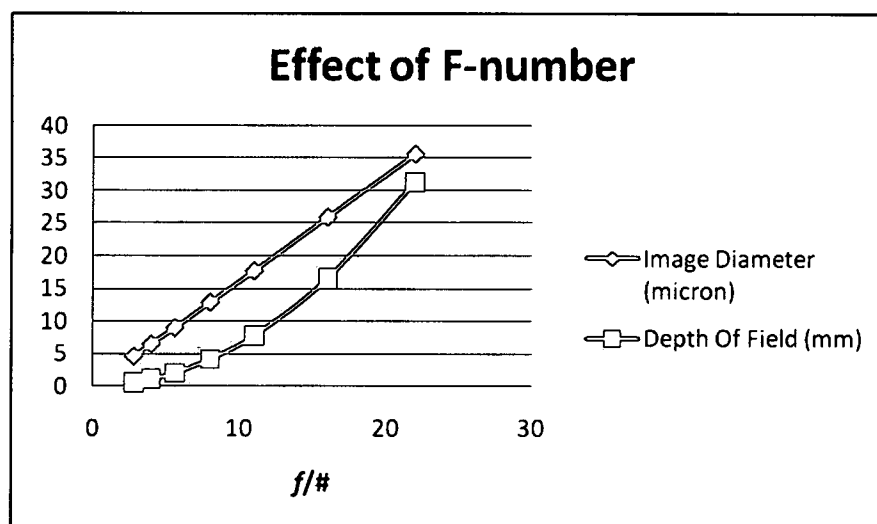


Figure 2.15: Plot showing the effect of $f/\#$ on DOF and the particle image diameter.

Chapter 3

EXPERIMENTAL SETUP

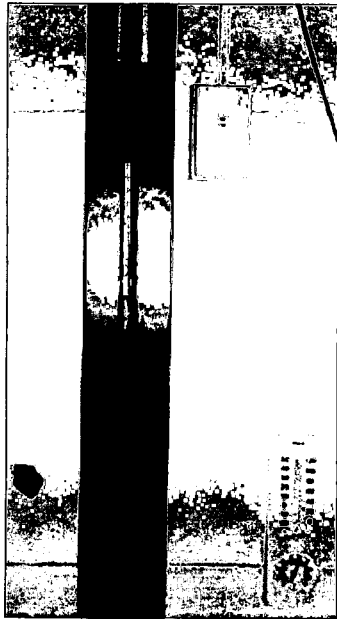
3.1 Facility

All experiments were conducted in the University of Dayton (UD) Low Speed Wind Tunnel (LSWT) facility. The UD-LSWT is an Eiffel type wind tunnel with 30" \times 30" \times 90" test section. Six anti-turbulence screens ahead of the converging section of this LSWT reduce velocity components in the flow that are parallel to the axis of the wind tunnel and greatly dampen variations in the longitudinal direction. This draw-through type wind tunnel, with a contraction ratio of 16:1 can achieve speeds up to 120 ft/s in the test section. A turbulence intensity of 0.035% was measured by hot-wire in the wind tunnel test section.

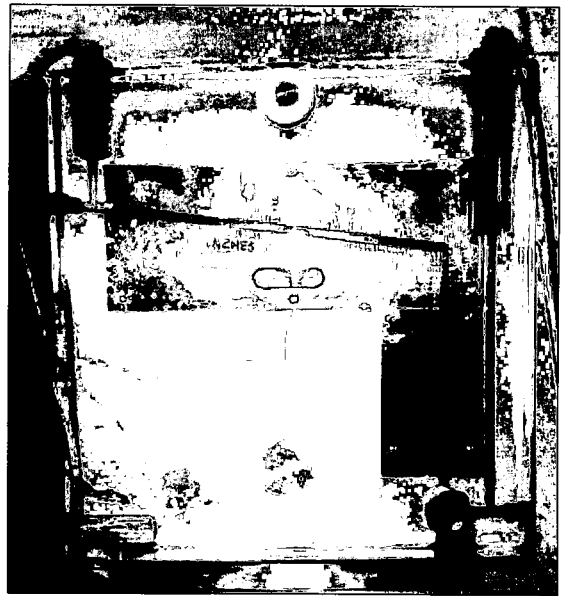
Environmental conditions have influence on any experiment; at the UD-LSWT a traditional barometer, thermometer and a hygrometer shown in Figure 3.1a are manually checked every 15 minutes for any variation in these conditions. These conditions are then used as an input to an indigenous LabView program (Screen shot shown in Figure 3.2) in the UD-LSWT facility, which then gives the new conditions for the wind tunnel to maintain a constant Reynolds number for the experiments. A Pitot static tube is located near the inlet of the test section to measure the speed of the incoming undisturbed flow. The conditions from the LabView output are verified with the manometer reading (Figure 3.1b) and the fan rpm is adjusted to get to the required setting.

3.2 Equipment for Experiments

The Particle Image Diagnostic Techniques (PDIT's) use a light source, high speed digital camera, pulse generator, particle seeder and a computer with camera software.



(a)



(b)

Figure 3.1: (a) Shows the traditional mercury barometer and the thermometer with hygrometer, (b) Image shows the u-tube section of the manometer hooked up to the pitot static tube.

3.2.1 High Speed Camera

Experiments were conducted using a pco.1600 (Figure 3.3) camera from The Cooke Corporation and requires a computer with a minimum of 1.6 GHz processing speed, 256 MB RAM and Windows XP with Service Pack 1 or higher. The complete

pco.1600 camera has two parts, the camera/exposure control unit and the control box/power supply.

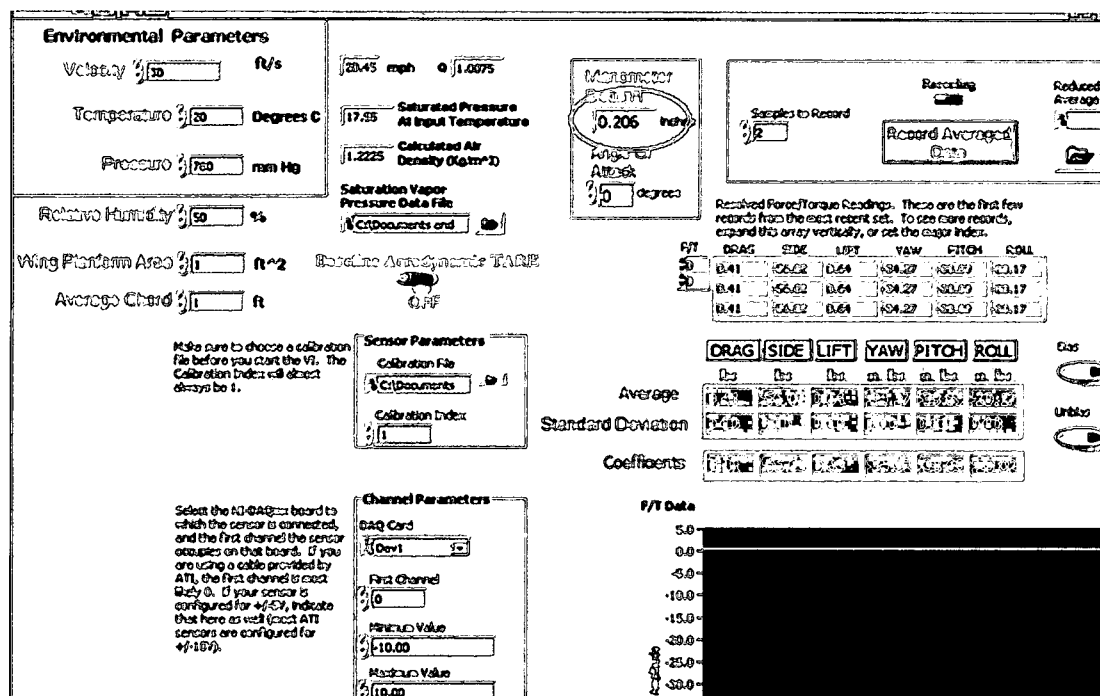


Figure 3.2: Image shows the screen shot of the Labview program with the inputs on the left under environmental parameters and the highlighted output as the required manometer reading.

The pco.1600 has a 1600×1200 pixel monochrome Charge-Coupled Device (CCD) array with 1 GB onboard memory and uses a firewire interface for data transfer. The lens is mounted using a C-mount. The pco.1600 has a peak quantum efficiency of 55% at 500 nm and has a spectral range of 300 - 1000 nm. The full well capacity of the CCD array is 40,000 e^- before saturation. The camera has a maximum dynamic range of 72 dB and a 14 bit pixel analog to digital range (A/D).

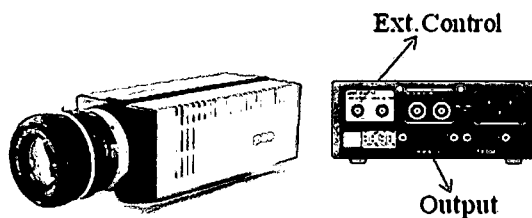


Figure 3.3: Left to right, The pco.1600 camera and the control box from The Cooke Corporation.

The pco.1600 has a 24-40 W power consumption supplied from the control box or the power supply unit in a pco.1600. The power supply unit also receives input from the internal (software) or external Transistor-Transistor Logic (TTL) signal to control the speed of the camera and the exposure time of the first image. The control box is also used to regulate the sensor temperature between 5-40 °C.

Inside the camera the light is converted into electric charges using the CCD array and then into the digital signals. The CCD array is a collection of light-sensitive diodes, called photosites, or pixels, which are a few microns in size, that convert light (photons) into electrical charges called electrons. Each pixel is light sensitive, and the charge produced is proportional to the brightness of the light striking them. These charges are stored as analog data that are then converted to digital via a device called an analog to digital converter (ADC). These digital signals are then transferred to the onboard memory of the camera. Figure 3.4 shows the working structural overview of the system.

3.2.2 Light Source

The PIDT's Particle Image Velocimetry (PIV), Volume Illuminated Forward Scatter PIV (VIFS-PIV) and Particle Shadow Velocimetry (PSV) are used for flow diagnostics on the sampling probe. PIV and VIFS-PIV use a high energy coherent light source (Nd:YAG laser) whereas PSV uses an incoherent low energy light source (LED).

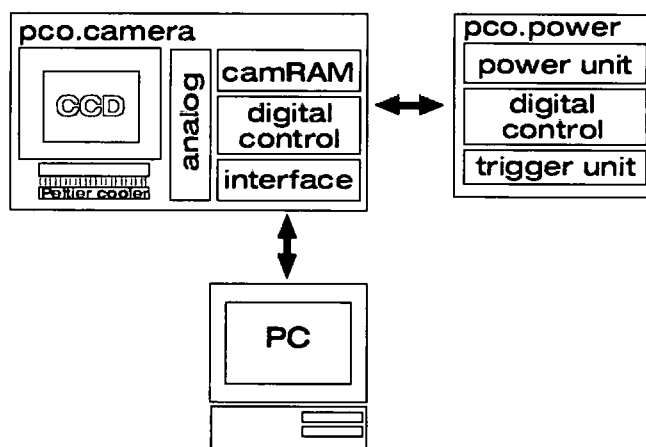


Figure 3.4: Structural overview of the pco.1600 camera system.

Light Source for PSV

The PSV technique uses an inline illumination technique which requires a low energy light source. The LM2 RGB (Figure 3.6a) series used in the experiments by Innovative Scientific Solutions, Incorporated (ISSI) has three colored LED's. The greatest output intensity for the LM2 RGB is achieved if the duty factor is limited to 5% and the maximum pulse width is < 3 msec. The LM2 RGB has a built in safety circuit to protect the illuminator if these limits are exceeded. Each color LED

is controlled by an input signal obtained from the BNC cable connected to the delay generator.

Table 3.1: PSV light source specifications

Wavelength - red	625 nm
Wavelength - green	530 nm
Wavelength - blue	460 nm
Pulsed - rise time	< 50 nsec
Pulsed - fall time	< 50 nsec
Minimum pulse width	140 nsec
Power-supply voltage	48 vdc/1.25 A

Light Source for PIV and VIFS-PIV

The PIV and the VIFS-PIV techniques use a high energy coherent light source. The ability to emit monochromatic light with high energy density makes the laser an ideal choice as the light source. Neodymium doped Yttrium-Aluminum-Garnet (Nd:YAG) lasers are widely used for PIV applications.

A New Wave Research Solo PIV Nd:YAG 120 laser was used in the experiments at the UD-LSWT. The Solo is composed of two components; the laser head, and the power supply.

The schematic of the laser head of the Solo is given in Figure 3.5. The standard Solo is a dual head laser with second harmonic. The Solo generates radiation of 1064 nm with the help of a dual flash lamp-pumped Nd:YAG rod. The second harmonic is generated by passing the InfraRed (IR) beam through the Potassium Titanium Oxide Phosphate (KTiOPO₄, KTP) crystal. The Solo uses the Type II matching in the KTP crystal. The type II crystal is used to generate green light of identical polarization. Dichroic mirrors (Mirrors with significantly different reflection or transmission at two

different wavelengths) separate the second harmonic from the fundamental light and direct the beam to the output port.

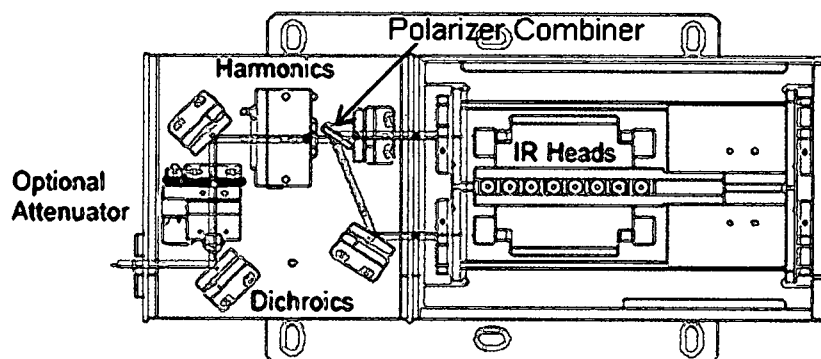


Figure 3.5: Schematic of the laser head of Solo PIV.

Table 3.2: Laser specifications

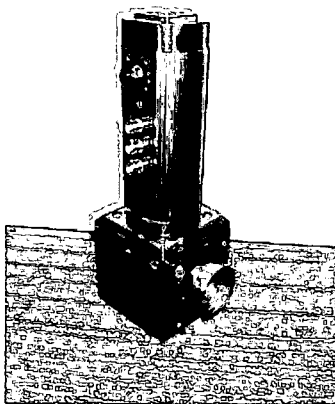
Energy	120 mJ/pulse
Stability	$\pm 4\%$
Pulse width	3-5 ns
Beam divergence	< 2 mrad
Beam pointing	$< 100 \mu\text{rad}$
Jitter	± 0.5 ns
Beam Diameter	4.5 mm

The supply unit houses the control system and the power supply unit to the laser. The power supply unit is built into three levels; 1) logic level electronics, 2) high voltage power supply and the simmer electronics, and 3) cooling system. The cooling system used in the Solo is closed loop and uses water. A water pump circulates the deionized water through the water-to-air heat exchanger. The water circulates through the laser head pump chamber to keep the YAG rod at acceptable

temperatures. The power supply unit also controls the firing of the laser. The laser can be externally controlled using the TTL signal.

3.2.3 Pulse Generation

A QC9614+ pulse generator (Figure 3.6b) from Quantum Composers was used to coordinate the timing between the camera and the light source. The QC9614+ pulse generator has a System Timer that functions as a non-retriggerable, multi-vibrator pulse generator. This means that once the QC9614+ is triggered either internally by pressing the RUN button on the front panel or externally by providing an input pulse which produces pulses continuously depending on the mode (Table 3.3). The Channel Timer for the QC9614+ functions as a non-retriggerable, delayed, one shot pulse generator. This means that the timer will only generate one delayed pulse depending on the selected mode (Table 3.3) of operation for every start pulse received and will ignore any additional start pulse until the pulse is completed.



(a)



(b)

Figure 3.6: (a) LED light source, (b) Quantum composer.

The QC9614+ pulse generator has one input and four output BNC connectors. The input can be used as a trigger to the pulse generating sequence in the QC9614+ pulse generator. The QC9614+ can generate up to 4 pulses per T0 pulse. These four pulses can be routed through any or all channels of the output connectors. Different modes of function and the flexibility in the output mixing give a wide variety of operational capabilities. Pulses generated by the QC9614+ pulse generator also have the flexibility of individually synchronizing to any of the other pulses. The architecture of the pulse is shown in the Figure 3.7.

Table 3.3: QC9614+ function modes

Continuous	Once started generates T0 continuously	One Pulse per T0 pulse
Single Shot	One T0 pulse per start command	One pulse is generated only for the first T0 pulse
Burst	'n' T0 pulses per start command	One pulse is generated for the T0 Pulse for first 'n' times
Duty Cycle	Once started T0 pulses cycle on and off	One pulse is generated for the T0 Pulse for first 'n' times and inhibited for the next 'm' times. This repeats.

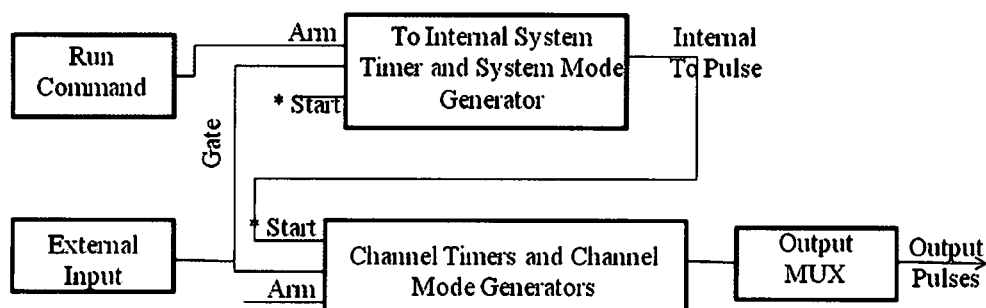


Figure 3.7: Architecture of the Pulse Generator.

3.2.4 Particle Seeder

In PIDTs flow properties are determined indirectly from the seed material. Different seed materials are used for different PDIT techniques. Talc powder is used as the seed material in PSV and smoke is used to seed the flow in PIV and VIFS-PIV.

Powder Seeder

A powder particle (Figure 3.8) seeder created by ISSI is used to seed the flow with the Talc powder ($\text{Mg}_3\text{Si}_4\text{O}_{10}(\text{OH})_2$). The particle seeder has two parts (the seeder and the control box). The control box is used for operating the seeder and controls the pressure in the system. It has three knobs to regulate the pressure in the shaker, purge and the blower lines. While using the powder seeder problems associated with clumping of talc need to be considered. Clumping of talc can be caused 1) due to the high moisture content in air and storing talc in the seeder for a long time or 2) due to the method of output of talc from the seeder. To overcome these problems talc should be replaced in the seeder before the experiment and a suitable output pipe that reduces clumping of talc should be used.



Figure 3.8: to right, particle seeder control box and particle seeder.

Smoke Generator

A LeMaitre G300 (Figure 3.9) is used to generate the smoke particles. The G300 is a microprocessor controlled, water based fog and haze generator. The fog fluid mixture (glycol and water) is vaporized by pumping through the heat exchanger. Under its own vaporization, the hot mixture is forced out of the output nozzle, where it mixes with air to form opaque aerosol (fog). The fog is made of tiny glycol particles ($1\text{ }\mu\text{m}$) that form around air. When suspended in air, the fog particles scatter the light. The G300 has a microcontroller which gives the capability to control the amount of smoke output but it is hard to control the quality of the smoke (density distribution or the direction of the flow).

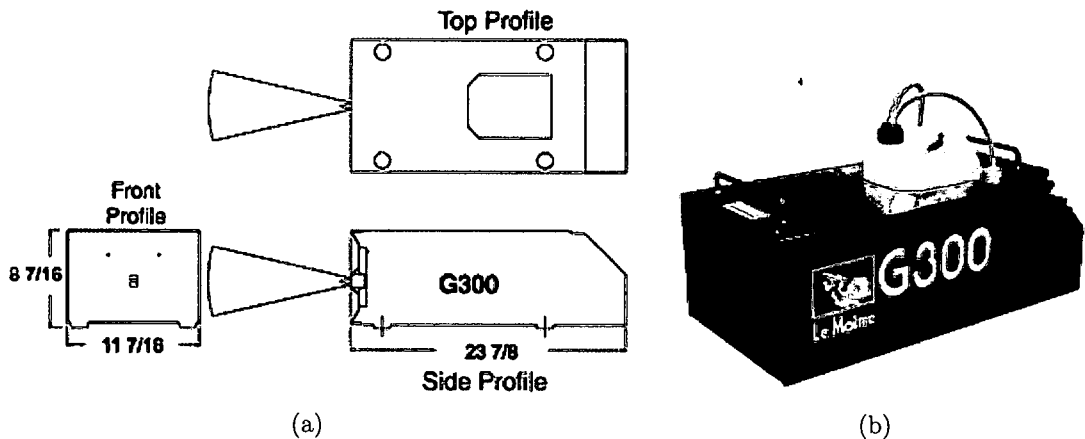


Figure 3.9: (a) Three views of the smoke machine, (b) LeMaitre G300.

3.2.5 Computer and the Camera Software

A Toshiba satellite 135-S4727 laptop with Windows Vista was used for the experiments. The camera software, pco.camware, was used to control the camera and

handle the data. The main function of the camera software is to aid in viewing the images from the camera. The images can be viewed in two modes:

1. the recording or the sequence mode where the images are recorded in the camera memory and recording is stopped once the memory is full
2. ring buffer mode where the images are recorded continuously.

The camera software provides the ability to control various camera properties. The camera can be internally or externally triggered, this feature of the camera is selected using the camera software. The size of the CCD array used can be varied using this software, which in turn decides the image capturing speed of the camera. The single image mode or the double image/PIV mode of the camera is also selected from the camware software.

3.3 Setup

This section explains the experimental setup used in the LSWT at UD. Figure 3.10 shows the top view of the setup.

3.3.1 Model Setup

The model was placed close to the inlet of the test section so that the incoming flow is undisturbed. A bread board is used to adjust the location of the model from the middle to the front of the test section (Figure 3.11a). The model is fixed on the top using a stainless steel support. Two clamps are used to get the model oriented in the direction of the flow and to give the flexibility to adjust the height.

The flow in the Field of View (FOV) is at least 10 probe diameters away from any interference/obstruction in the flow due to the wall or the fixtures.

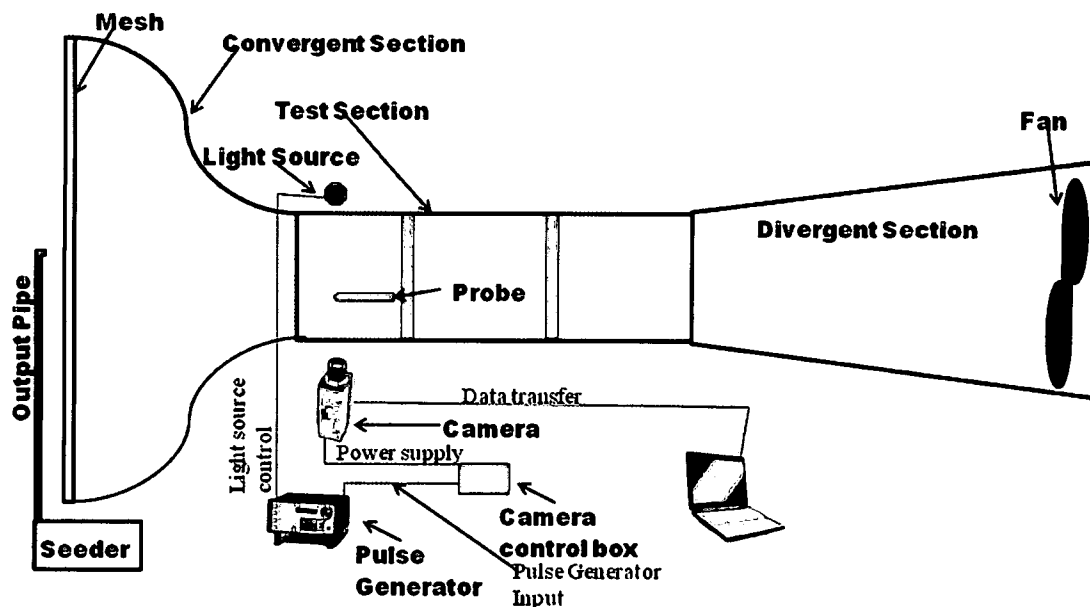


Figure 3.10: Top view of the experimental setup.

3.3.2 Camera Setup and Focus

The model of the probe considered for the experiments is cylindrical in shape, therefore a symmetrical flow is assumed about the axis of the probe. Because of the axisymmetry, flow is assumed to be two dimensional along any plane passing through the axis of the probe.

To study the near body flow at the tip of the probe using PSV, the camera was focused on the lower half of the probe tip with a Field of View (FOV) of $14.0\text{mm} \times 10.5\text{mm}$ (Figure 3.12). This FOV with a magnification of 0.85 was obtained using the

Nikkor 180 mm 1:2.8 D lens from Nikon with 15 cm of spacers between the camera and the lens. The aperture of the camera was completely open at an f-number ($f/\#$) 2.8 to collect enough light and also achieve a thin Depth of Field (DOF) (≈ 0.1 mm). In VIFS-PIV a FOV of $32\text{mm} \times 24\text{mm}$ with a magnification of 0.37 was obtained using the Nikkor AF micro 1:4 D 105 mm lens from Nikon with 6 cm of spacers. The aperture of the camera was completely open at an $f/\#$ 4.

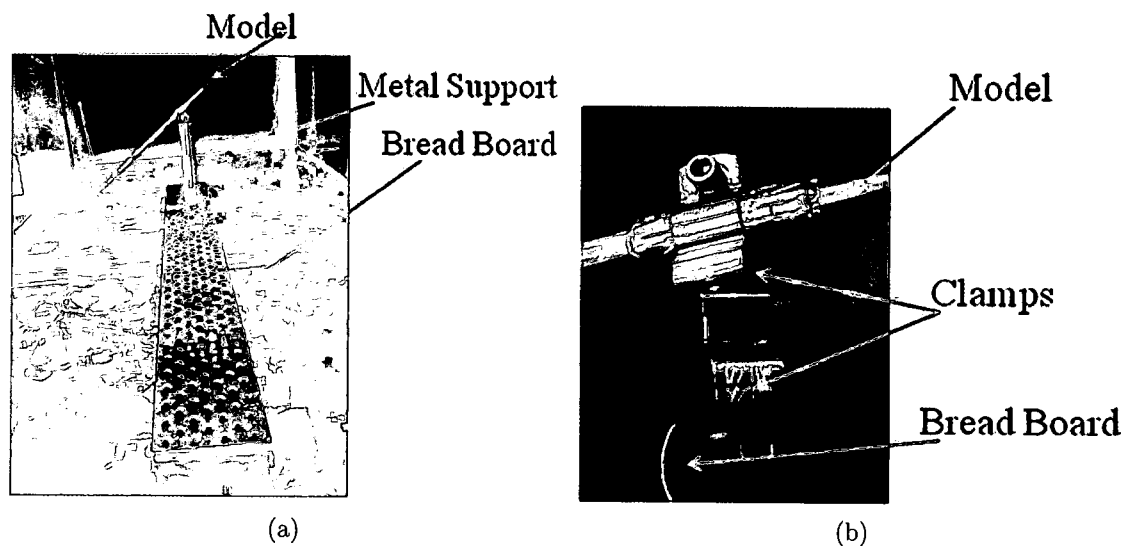


Figure 3.11: (a) Model placed close to the inlet of the test section using a bread board, (b) Model fixed to the metal post with the help of clamps.

In PIV a FOV of $19.3\text{mm} \times 14.5\text{mm}$ with a magnification of 0.61 was obtained using the Nikkor 180 mm 1:2.8 D lens from Nikon with 12 cm of spacers between the camera and the lens. The aperture of the camera was completely open at an $f/\#$ 2.8.

The Camera was placed 0.5" away from the side wall of the wind tunnel test section in both the PSV and VIFS-PIV experiments. In PIV a thin laser sheet is

formed in the plane of the FOV and the camera is focused perpendicularly to the FOV as seen in Figure 3.13. The possible orientation of the sheet forming optics limited the manner in which the light sheet was brought into the test section. This limitation resulted in bringing the light sheet in through the side wall and resulted in the camera being moved to the top of the test section (Figure 3.13).

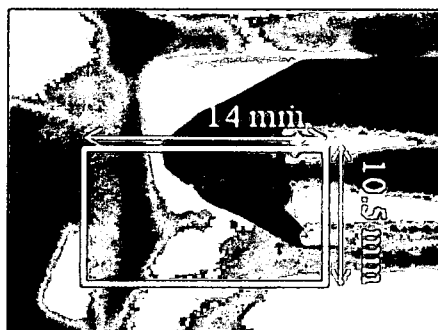


Figure 3.12: Specially designed target, 14.0 mm wide and 10.5 mm high.

3.3.3 Light Source Setup

In PSV the LED light source is placed in line with the FOV and the camera on the far side of the wind tunnel. All the LED's of the three color LED light source were fired simultaneously during the experiments for a brighter FOV. The three BNC connectors can be seen in Figure 3.6a.

An Nd:YAG laser was used as the light source in the VIFS-PIV experiments. Figure 2.12 shows the schematic of the VIFS-PIV experiments. Direct exposure of the camera sensor can cause damage therefore the FOV is illuminated at an angle.

Figure 3.13 shows the schematic of the PIV experimental setup. A laser beam is spread into a horizontal light sheet in the plane of the FOV using a prism and a

cylindrical lens. A camera is placed on the top of the test section to focus on the FOV.

3.3.4 Target and FOV

A target was designed to help focus the camera on a FOV in the desired plane. Figure 3.14a shows the designed target. The Pin attached to the target is placed in the aspiration hole (Figure 3.14b) of the probe and the weight is left to hang on its own. This allows the target plane to align vertically with the vertical plane of the probe. Now the camera is focused on the target to get the desired FOV. The width of the special target is 14.0 mm and each horizontal line is spaced 0.5 mm apart.

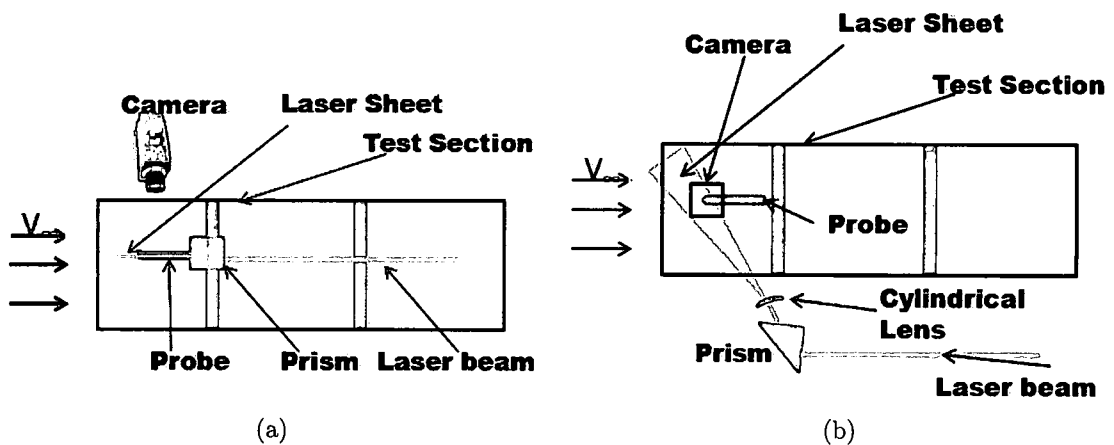


Figure 3.13: (a) Schematic showing the side view of the PIV experimental setup, (b) Schematic showing the top view of the PIV experimental setup.

3.3.5 Sequencing and Timing

Timing the camera and the light source simultaneously and sequencing the images correctly is important for any flow diagnostic technique. Though the basic

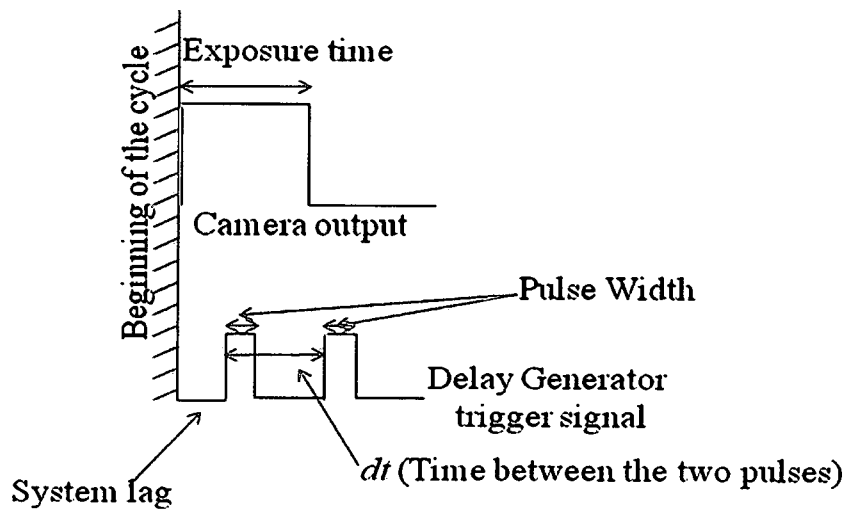


Figure 3.15: Timing sequence in PSV technique.

Timing in PIV and VIFS-PIV

The triggering and the timing of the experiments in PIV and VIFS-PIV is controlled by the delay generator. The timing sequence between the camera and the laser is shown in Figure 3.16.

The camera in these experiments uses the trigger to capture image pair and the exposure time of the images is controlled by the camware software. The input from the delay generator triggers one cycle of image capture. Using the camware the software exposure time for the first image can be defined but the exposure time of the second image cannot be controlled due to the CCD camera limitations.

Four trigger signals are required to control the laser externally; two to trigger each laser flash lamp and two to trigger each Quality switch (Q-switch). Laser lamp one (L1) and Q-switch one (Q1) are associated with first laser head and laser lamp two (L2) and Q-switch two (Q2) are associated with the second laser head. The first

trigger signal from the delay generator triggers L1 and after a Q-switch delay of dt_{Q1} Q1 is triggered. L2 is triggered after a time delay of dt , with respect to L1, which is the time between two consecutive images. Q2 is triggered after a Q-switch time delay of dt_{Q2} , with respect to L1. To have same power in both the laser pulses $dt_{Q1} = dt_{Q2}$.

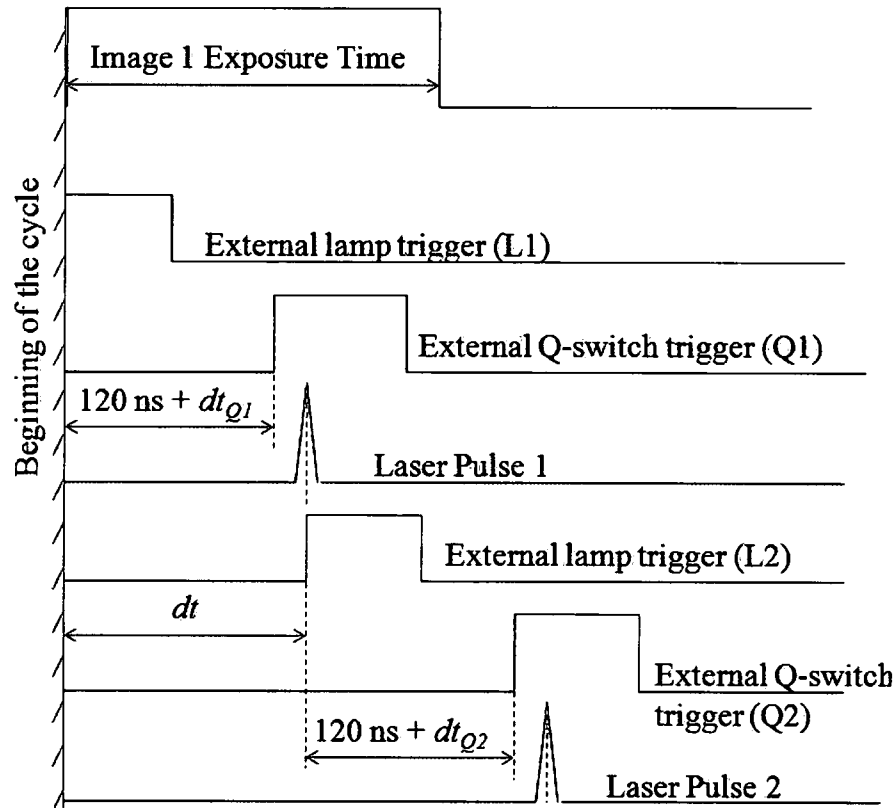


Figure 3.16: Timing sequence in PSV technique.

Data taken using the experimental setup explained in this chapter is analyzed and discussed in the next chapter.

Chapter 4

RESULTS AND DISCUSSION

A numerical investigation was conducted at the US Air Force Research Laboratory (AFRL) Propulsion Directorate on a particulate sampling probe with conditions similar to a gas turbine at idle. Experiments to study the near body flowfield on the probe were conducted at the University of Dayton Low Speed Wind Tunnel (UD-LSWT). To match the experimental conditions at the UD-LSWT with the numerical investigation done at AFRL, experiments were conducted at a Reynolds number (Re) of 22,000. All the experiments used a pco.1600 camera with a 180 mm lens with an F-number ($f/\#$) 2.8.

Three different Particle Image Diagnostic Technique's (PIDT's), Particle Shadow Velocimetry (PSV), Volume Illuminated Forward Scatter Particle Image Velocimetry (VIFS-PIV), and Particle Image Velocimetry (PIV), were used to investigate the near body flowfield of the probe. Captured images were then analyzed using DPIV 2.1 analysis software created by Innovative Scientific Solutions, Incorporated (ISSI). The results from these experiments are discussed and compared.

4.1 Theoretical Estimation of the Boundary Layer Thickness

Due to the cylindrical shape of the probe, an axisymmetric flow is assumed near the probe tip. Considering any axial plane of the probe, the probe tip would have a wedge shape. The boundary layer on the probe tip can be estimated using the

Falkner-Skan equations. The momentum thickness and the displacement thickness from Falkner-Skan theory are given by:

$$\eta^* = \int_0^\infty (1 - f') d\eta = (\eta - f)_{\eta \rightarrow \infty} \quad (4.1)$$

$$\theta^* = \int_0^\infty f'(1 - f') d\eta = \frac{f_0'' - \beta \eta^*}{1 - \beta} \quad (4.2)$$

where, η^* and θ^* are the momentum and the displacement thickness, f^* is defined as the ratio of the velocity to the freestream velocity, η is the function defined by $yg(x)$ and $\beta\pi/2$ is the half wedge angle (Figure 4.1).



Figure 4.1: Wedge half angle of the particulate sampling probe.

Figure 4.1 shows the wedge half angle of the sampling probe. With the wedge half angle of 37° , β for the probe is 0.4. The Falkner-Skan equation (Eq. 2.9) is solved in MATLAB using the ode45 routine which is based on an explicit Runge-Kutta (4,5) formula with $\beta = 0.4$ substitution.

A wedge half angle for the probe is assumed constant in solving the Falkner-Skan equation. Figure 4.2 shows the plot of f' Vs η obtained from MATLAB using Excel. A sixth order polynomial curve fit with $R^2 = 1$ is also shown. A solution to this sixth order polynomial at $f' = 0.99$ (u/V_∞) gave four imaginary values, a negative value and a positive value. η cannot be an imaginary or a negative quantity as it is a

dimensionless number representing length. The solution to the sixth order polynomial equation gave $\eta = 2.65$.

In Figure 4.3, f and f'' are plotted against η and polynomial curves are fit. Substituting the value of η in these equations give the values of the functions f and f'' at $f' = 0.99$. The momentum and the displacement thicknesses for the boundary layer on the probe are calculated by substituting f , f'' and η in Eq.s 4.1 and 4.2. The calculated value of the displacement thicknesses just before the end of the conical section of the probe is 0.3 mm.

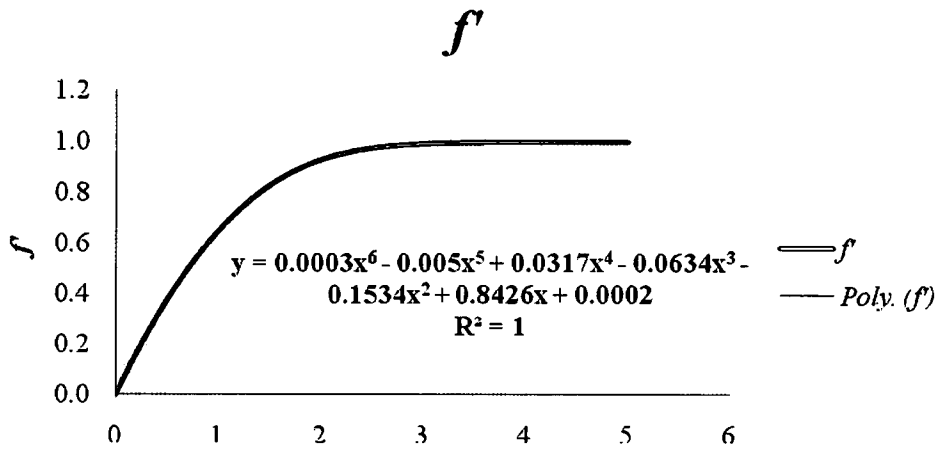


Figure 4.2: Theoretical velocity profile inside the boundary layer of the particulate probe.

4.2 Particle Image Diagnostic Techniques (PIDT's) Data Analysis

Images obtained from the three PIDT's, Particle Shadow Velocimetry (PSV), Volume Illuminated Forward Scatter Particle Image Velocimetry (VIFS-PIV) and Particle Image Velocimetry (PIV), are analyzed using the DPIVB software developed

by Innovative Scientific Solutions, Incorporated (ISSI). The size of the interrogation region depends on the particle image density, estimated local velocity gradients, particle-image size, and the desired spatial resolution. The peak of the correlation map corresponds to the average velocity displacement within the interrogation domain. An intensity-weighted peak-searching routine is used to determine the location of the peak to sub-pixel accuracy. The software includes a grid feature that allows selection of areas of the image to be processed. This permits removal of solid regions as well as shadows from the processing areas, provides a choice of various correlation engines and correlation peak locators, and incorporates several improvements to standard (single-pass) PIV techniques such as recursive estimation of the velocity field through a multipass algorithm for increasing accuracy and resolution. [6, 7, 23]

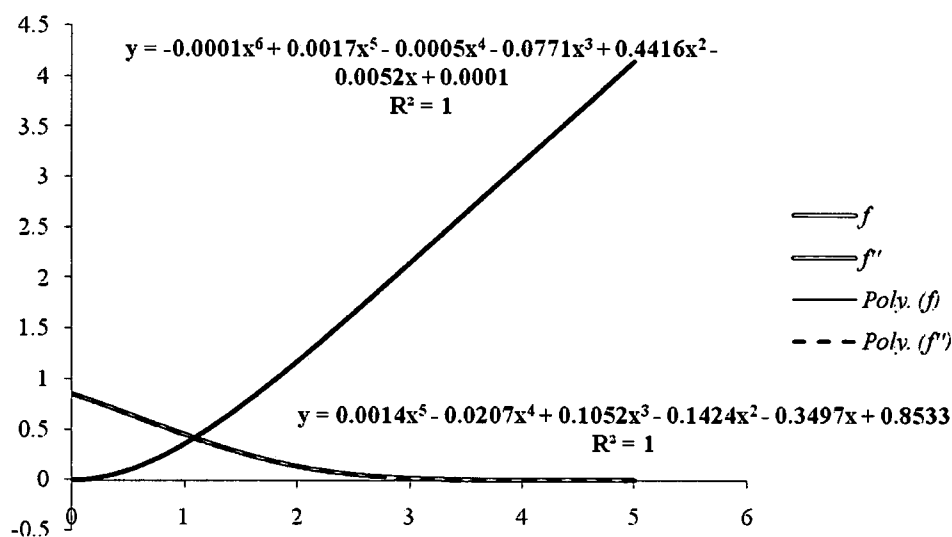


Figure 4.3: Variation of the functions f and f'' with β .

During the analysis a 75% overlap of the neighboring interrogation regions was used. Overlapping the interrogation regions include many of the same particles in five neighboring correlation maps which when multiplied yield a single correlation map with lower noise; this filter used in the analysis is called the Correlation Multiplier.

During the post processing of the image data, three filters were used to reduce outliers from the data. First the nearest neighbor filter compares the velocity vector obtained in an interrogation region with the nearest neighbor; if a dramatic difference is found between the vector and the neighboring vectors then the vector obtained in the interrogation region is determined as an outlier and eliminated from the data. Application of this filter can result in loss of data at sharp corners where there is a sudden change in the direction of the flow. Because this kind of a flow is not expected in the current experiment application of this filter does not result in loss of any data.

The other two post processing filters, Vector Length Cutoff (VLC) and the Velocity Direction Filter (VDF), are a little similar in a nature. Application of these filters need a priori estimation of the size and direction of the flowfield which can be obtained from a preliminary analysis of a pair of images without the filters. The VLC filter in the DPIVB software determines that any vector value larger than the estimated maximum vector size as an outlier/bad data and the vector is eliminated from the data. Similarly, the VDF filter has a range of permissible values in both axes. Any velocity data that have the velocity component in any direction outside of these ranges is determined an outlier and eliminated from the data.

4.3 Particle Shadow Velocimetry (PSV)

Experiments using the PSV technique used three Light Emitting Diodes (LED's) simultaneously in order to volumetrically illuminate the flowfield near the probe tip. Seed materials used included talc, glass balloons and phenolic resin particles. A Field Of View (FOV) of 14mm \times 10.5mm was obtained in the PSV experiments.

Images were captured at the full sensor size (1600 \times 1200 pixels) of the camera. The camera sensor is 11.84 mm \times 8.88 mm with each pixel 7.4 μ m \times 7.4 μ m in size. This indicates that the magnification factor of 0.85 was achieved during the PSV technique.

During the PSV experiments 15 cm of spacers were used between the camera and the lens which tend to increase the Depth Of Field (DOF) of the images. A completely open lens aperture at $f/\#$ 2.8 tends to keep the DOF small. The PSV experimental setup gave a DOF of 0.08 mm. This was calculated using Eq. 2.23.

$$\delta_z = 4(1 + M^{-1}) \left(\frac{F}{A} \right)^2$$

Four sets of experiments were conducted using the PSV technique. In two of the four sets of experiments, the flow was seeded with talc, one with glass balloons and one with phenolic resin. The two experiments that used talc as the seed material varied in the powder seeder setting. The first experiment used a 0.5" diameter outlet pipe and the second experiment was performed using a 0.25" outlet pipe. Changing the outlet pipe diameter from 0.5" to 0.25" reduced the clumping of talc and led to smaller particles in the flowfield. In these experiments the camera was internally triggered to acquire the images.

Figure 4.4 shows a raw image from the PSV experiment with a 0.5" diameter pipe outlet on the powder seeder. Shadows of the probe tip and the individual particles are seen. In Figure 4.4 dark particles are imaged on a bright background in contrast to many PIDT's where the scattered light from the particles is captured on a dark background. An even distribution of the seed material in the entire FOV is obtained. A difference in brightness is found in the raw image; this is clearly noticed in Figure 4.5. The difference in brightness is caused by a difference in the offset in two Analog to Digital Converters (ADC) in dual ADC mode. Sensitivity of the ADC's change with aging.

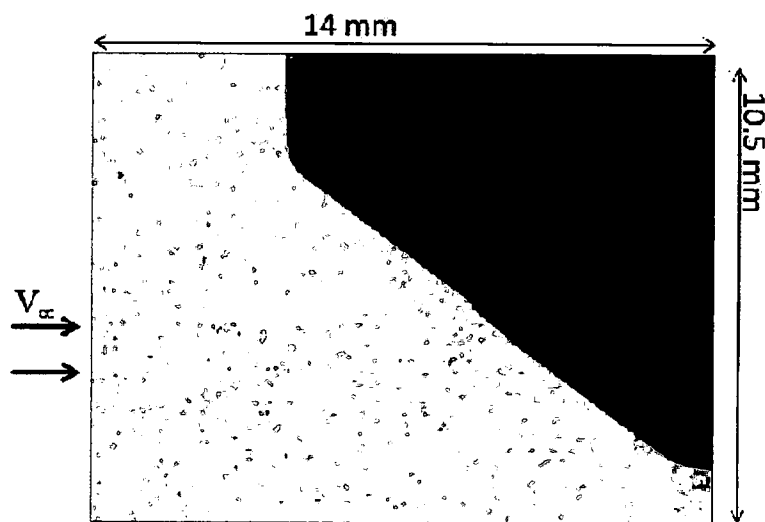


Figure 4.4: Raw image captured using the PSV technique showing the shadows of the probe tip and the particles on a bright background.

The velocity distribution obtained from a pair of images using DPIV is shown in Figure 4.5. Each image was divided into interrogation regions with 32×32 pixels and with a 50% overlap with the neighboring interrogation regions. A smaller FOV

was not possible as each interrogation region had 7 to 8 particles. This meets the recommended criteria of 7 particles per interrogation region when using the cross correlation method for data extraction from the images.[12]

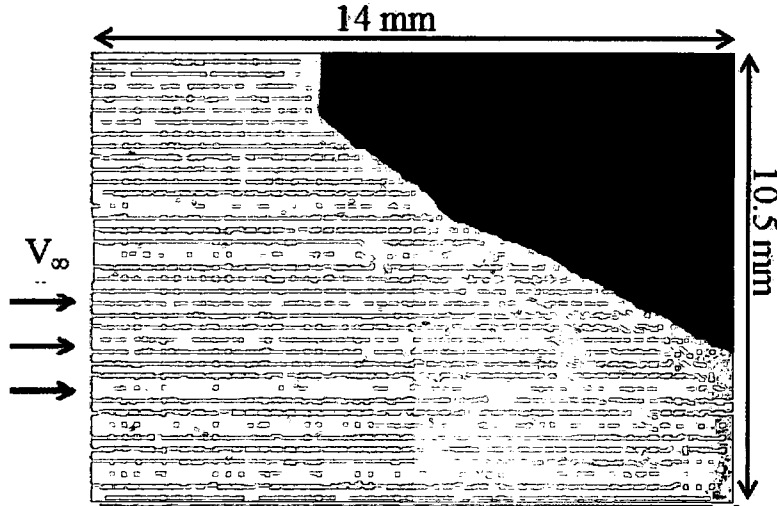


Figure 4.5: Velocity distribution obtained from processing a pair of PSV images seeded with talc shows biased velocity data due to the particle inertia and also shows two different brightness's from the two camera ADC's.

Data from more than 50 images pairs is averaged to plot the velocity contour (Figure 4.6). Streamlines drawn from the velocity data are also seen. Streamlines are expected to curve ahead of the probe, but in Figure 4.6 they are heading straight into the probe. Slight curving of streamlines is noticed only at the outer diameter of the probe.

An unexpected straight flow is noticed in Figure 4.6 which can be explained using the Stokes number (Stk). Talc particles in Figure 4.4 have an average size of $30 \mu\text{m}$, density of talc is 2700 Kg/m^3 , and the freestream velocity is 21.5 m/s . Substituting these parameters in Eq. 2.19 gives a Stokes number 11.3. Stokes number should be

$\ll 1$ for the seed material to follow the flow faithfully. The seed material in the first set of PSV experiments have a Stokes number of $11.3 \gg 1$ suggesting that the $30\text{ }\mu\text{m}$ size talc particles do not follow the flow faithfully.

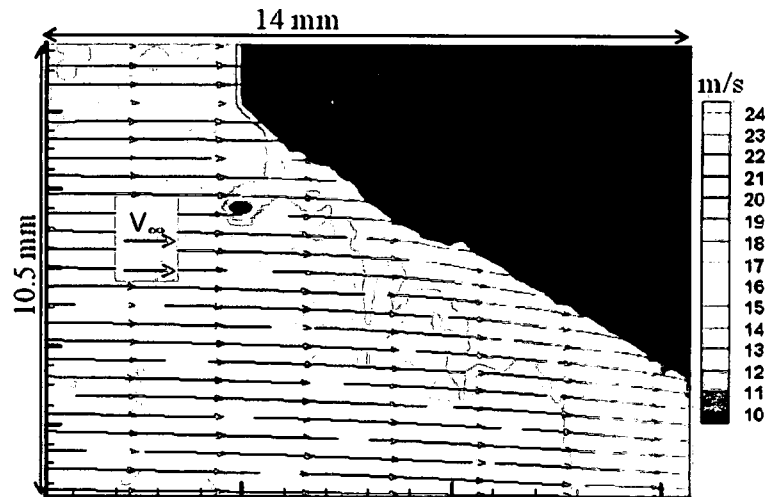
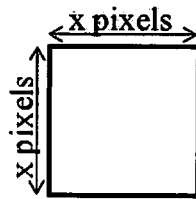


Figure 4.6: Velocity contour from PSV shows the averaged streamlines obtained from the biased velocity data resulting from the use of talc seed particles.

Response time for the talc particles with $30\text{ }\mu\text{m}$ diameter was 7.55 msec calculated from Eq. 2.16. The characteristic time of the flow defined as the ratio of the size of the interrogation region to the freestream velocity of the flow is $13.0\text{ }\mu\text{sec}$ (Figure 4.7). The calculated response time is about three orders higher than the characteristic time which is a further indication that the talc particles do not follow the flow faithfully.

With the 0.25" diameter seeder output pipe clumping of the talc particles was reduced compared to the 0.5" diameter output pipe resulting in smaller seed particles. The particle size was reduced to $10\text{ }\mu\text{m}$ with the modified seeder setup. Talc with a $10\text{ }\mu\text{m}$ particle size has a Stokes number of 1.2 which is >1 and does not satisfy the

Stokes number criteria for the seed particles to follow the flow faithfully. Response time for the particles with the modified experiments is 0.84 msec which is about two orders higher than the characteristic time suggesting that the 10 μm talc particles do not follow the flow.



$$\text{Characteristic time} = \tau_f = x \text{ size of the pixel} / (M \times V_\infty)$$

Figure 4.7: The relation between the size of the interrogation region, free stream velocity and the characteristic time.

In the third and fourth sets of PSV experiments, flow was seeded with the phenolic resin particles and the glass balloon particles respectively. Figure 4.8a shows the instantaneous flowfield velocity data from the flow seeded with phenolic resin particles. Figure 4.8b shows the extracted velocity data from a pair of images of the flow seeded with glass balloons. In both figures arrows are shown where the flow starts to curve. This is much later than where the flow is expected to turn.

The size of the phenolic resin particles vary between 5 and 20 μm and the size of the glass balloons is 10 μm . Densities of the phenolic resin particles and the glass balloons are 1300 kg/m^3 and 500 kg/m^3 respectively. The Stokes number and the response time for the phenolic resin particles vary between 0.15 and 2.43, and 0.1 and 1.6 msec respectively. The Stokes number and the response time for the glass balloons

are 0.23 and 0.15 msec. Response times for both of the seed materials are higher than the characteristic time indicating that they do not follow the flow faithfully.

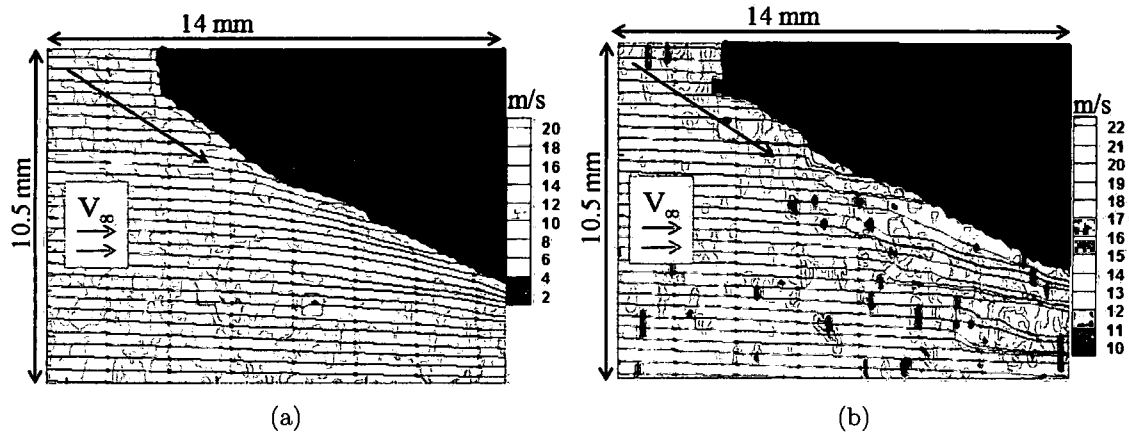


Figure 4.8: (a): Averaged streamlines from 5 pairs of images with flow seeded with phenolic resin particles, (b) averaged streamlines from 4 pairs of images with flow seeded with glass balloons. Both images show a biased velocity data and curving of streamlines much later than they are expected.

4.4 Volume Illuminated Forward Scatter Particle Image Velocimetry (VIFS-PIV)

VIFS-PIV experiments used a New Wave Research Solo PIV Nd:YAG 120 laser for the light source and smoke was used to seed the flowfield. A FOV of 18.6 mm \times 14 mm was used during the VIFS-PIV experiments.

Images were captured at the full size of the camera sensor. A magnification factor of 0.63 was obtained in capturing the images using the VIFS-PIV technique. From Eq. 2.23 the DOF for the experiments is 0.11 mm.

Figure 4.9 shows the raw image captured using the VIFS-PIV technique. The smoke particles in the image are finer and smaller. The smoke particles have a typical

diameter of $1\ \mu\text{m}$ and a density of $1037\ \text{Kg/m}^3$. The Stokes number and the response time, calculated from Eq.s 2.18 and 2.15, for the experiments were 5×10^{-3} and $3.2\ \mu\text{sec}$ respectively. The Stokes number for the smoke in the VIFS-PIV technique satisfies the criteria ($Stk \ll 1$) and the response time is shorter than the characteristic time ($16.7\ \mu\text{sec}$) of the flow. These values for the Stokes number and the response time indicate that the smoke follows the flow faithfully.

Figure 4.12 shows the streamlines obtained from velocity data from images taken using the VIFS-PIV technique. The images were processed with a 32 pixel interrogation window size to estimate the behavior of the smoke particles in the flow. As expected, the velocity vectors can be seen turning ahead of the tip of the probe.

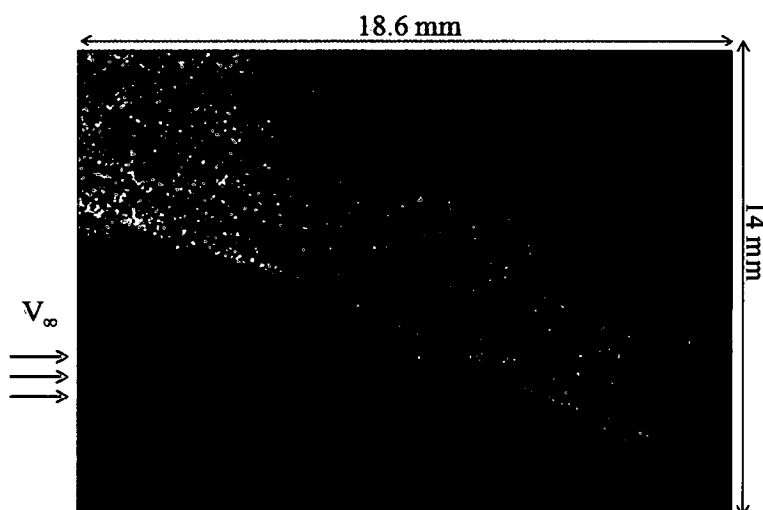


Figure 4.9: Raw image captured using the VIFS-PIV technique.

Figure 4.10 shows the comparison between the velocity data obtained from the same pair of images. In Figure 4.10a a 32 pixel interrogation region was used whereas in Figure 4.10b a 16 pixel interrogation region was used. Though a good distribution

of the seed particles is seen in Figure 4.7, decreasing the size of the interrogation region to 16 pixels causes a loss of the velocity data. Volume illumination of the VIFS-PIV technique not only illuminates the seed particles in the plane of interest but also particles out of this plane. Because the position of the smoke in the wind tunnel cannot be controlled, the smoke particles move in the illuminated volume. The coherent light scattered from the out-of-plane particles create speckle noise in the images.[17] Figure 4.11 shows two images, the raw image and the modified brighter image of the same sample image. The intensity of the image does not have any influence on the cross-correlation peak.[6] Thus the speckle noise in the image reduces the number of detectable particles in the image restricting the analysis to 32 pixel resolution.

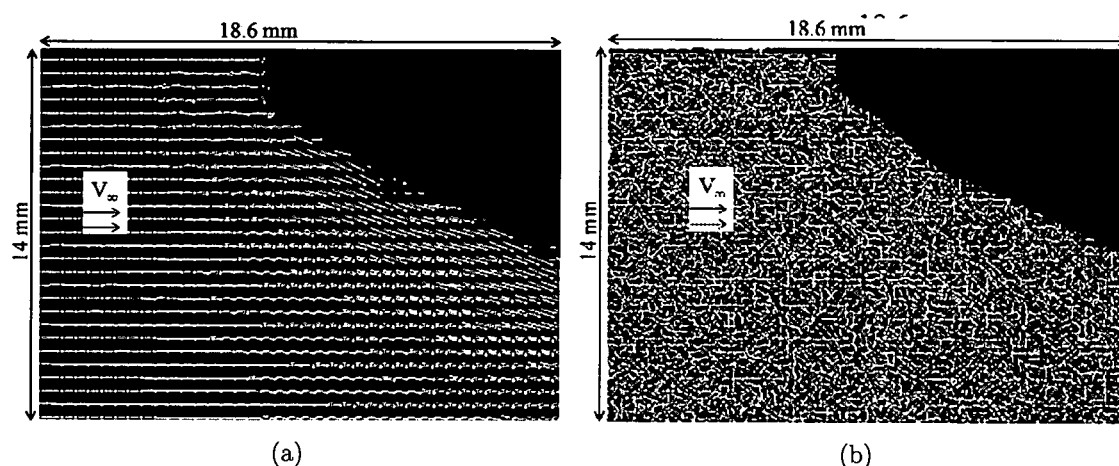


Figure 4.10: (a) Velocity data obtained from a pair of images with a 32 pixel interrogation region, (b) Velocity data obtained from a pair of images with a 16 pixel interrogation region. These images show that in a 16 pixel interrogation region there are fewer number of detectable particles than the minimum number of particles required for the cross-correlation method.

Images from the VIFS-PIV experiments were divided into 32×32 pixels interrogation regions with a 75% overlap with the neighboring interrogation regions. Velocity data from more than 50 pairs of images is averaged to plot the velocity contour (Figure 4.12). Streamlines in this image curve ahead of the probe as expected. The resolution of the velocity data is restricted by the size of the interrogation region.

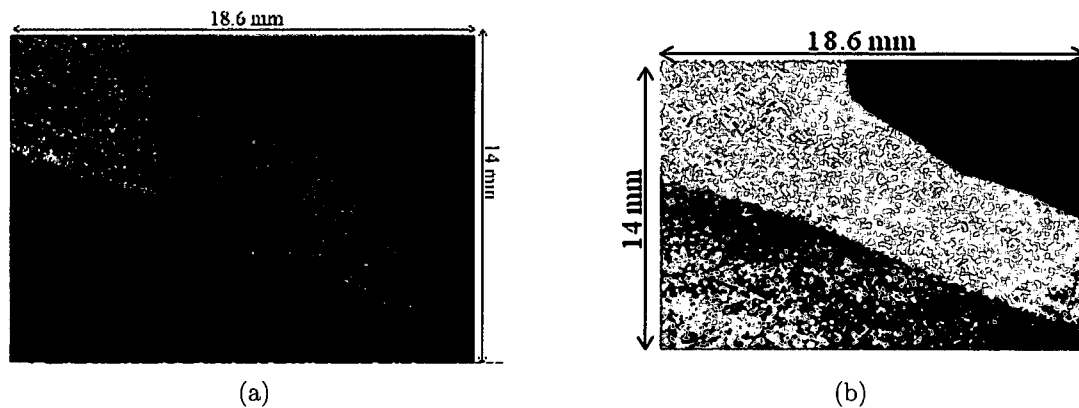


Figure 4.11: A brighter image of Figure 4.7. Brightening the image shows the speckle noise in the image.

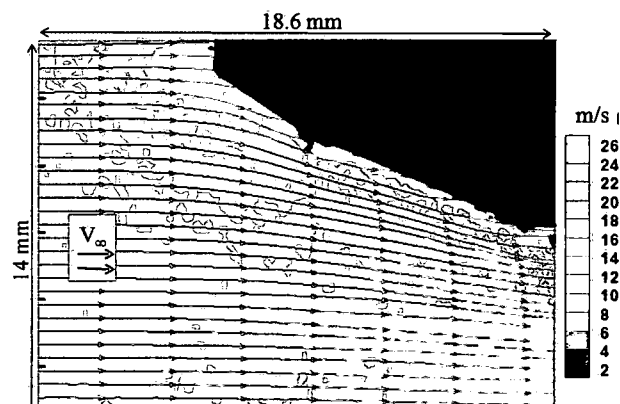


Figure 4.12: Velocity contour developed from the data obtained from VIFS-PIV shows streamline curvature as would be expected from a flowfield ahead of the probe.

4.5 Particle Image Velocimetry (PIV)

A New Wave Solo PIV Nd:YAG 120 laser is used as a light source to illuminate the flow seeded with smoke in the PIV experiments. A FOV of $19.3 \text{ mm} \times 14.5 \text{ mm}$ was imaged using a 180 mm lens at an $f/\#$ of 2.8. Images were captured at full camera sensor size with a magnification of 0.61 and a DOF of 0.11 mm.

Raw images obtained from the PIV technique are shown in Figure 4.13. The Stokes number and the response time, calculated from Eq. 2.19 and 2.16, for the PIV experiments are 5×10^{-3} and $3.2 \mu\text{sec}$. The Stokes number for the smoke in the PIV technique satisfies the criterion ($Stk \ll 1$) and the response time is smaller than the characteristic time ($8 \mu\text{sec}$) of the flow. These values of Stokes number and response time indicate that the smoke follows the flow faithfully.

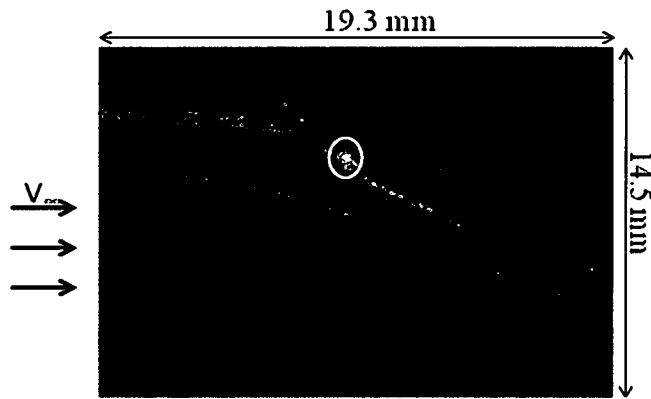


Figure 4.13: Raw image obtained from the PIV technique with the strong reflection area highlighted.

A small highlighted area is shown in Figure 4.13 denoting a reflection from the surface of the probe. Care should be taken during the experiments to keep the reflections below saturation levels of the charge-coupled device (CCD) array of the

camera. Saturating the sensor with reflected light can cause permanent damage of the CCD array.

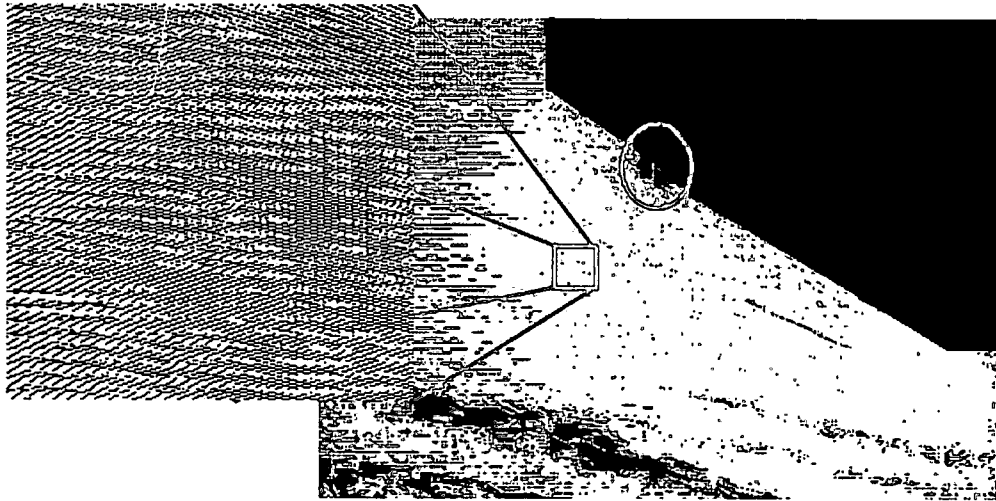


Figure 4.14: Velocity data obtained from a pair of PIV images at 16 pixel resolution, a zoom in window shows the density of the velocity vectors.

In Figure 4.14, velocity vectors over the entire FOV from a pair of PIV images are shown. PIV images are divided into interrogation regions of 16×16 pixels with a 75% overlap with the neighboring interrogation regions. A zoom-in in Figure 4.14 is showing a dense velocity vector data. A portion of the data at the bottom of the image is missing due to a lack of adequate seed particles in the region. The highlighted portion in the image also shows a loss of data; this is due to the reflection highlighted in Figure 4.13.

Figure 4.15 shows the contours of the velocity distribution and streamlines over the complete FOV. This image is generated by averaging 27 images in the DPIV software from ISSI. As expected, the streamlines are curved in this averaged image;

a small portion of the image is highlighted where the data were missing due to the reflections in the raw images captured with the PIV technique.

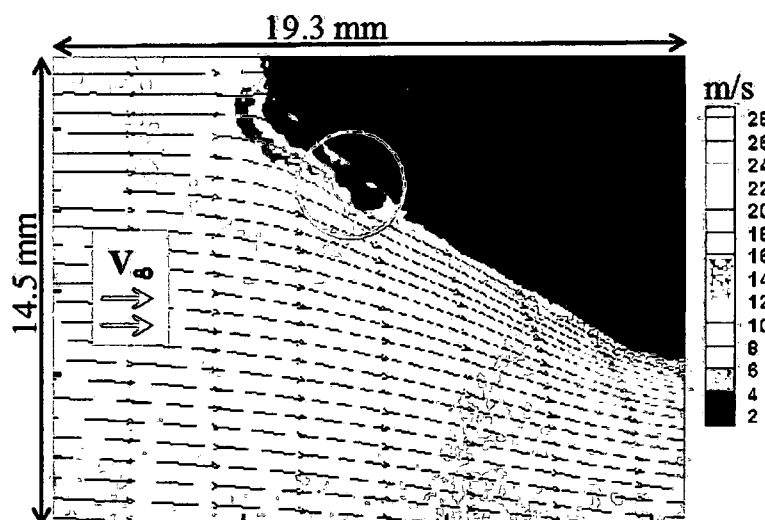


Figure 4.15: Velocity contour and the streamlines obtained from averaging 27 pairs of images from PIV showing the streamline curvature as would be expected from a flowfield ahead of the probe and loss of data due to reflection from the probe surface.

4.6 Comparison Of The Three Experimental Techniques

Comparison of the instantaneous raw images from the PSV, VIFS-PIV and PIV are shown in Figure 4.16. An even distribution of the seed material is seen in the three images. In Figure 4.16 instantaneous image from the PSV technique is seen. Due to the incoherent light used in the experiment, images captured from this technique do not have strong reflections from the surface and though the volume illumination method is used for illuminating the flow speckle pattern is not seen.

In VIFS-PIV usage of the coherent light source with the volume illumination is resulting in a speckle pattern. Though a coherent light source is used for illumination

the volumetric method of illumination does not show large reflections from the surface (Figure 4.16).

Use of PIV techniques to capture images does not have speckle pattern in the captured images. But the use of the high energy coherent light source causes reflections (Figure 4.16c) from the surface which has the potential to damage the camera sensor.

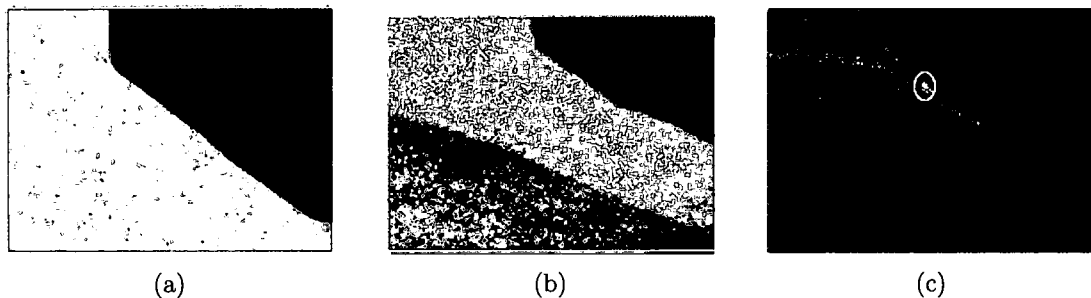


Figure 4.16: Instantaneous images from (a) PSV, (b) VIFS-PIV and (c) PIV.

To match the conditions of the experimental investigation conducted in the UD-LSWT with the numerical investigation conducted at AFRL, experiments were conducted at a Re of 22000. The freestream velocities in the three sets of experiments were different due to the environmental conditions. To compare the results from the three experiments the velocity distribution from each experiment is normalized by the freestream velocity over the entire FOV. Figure 4.17 shows the normalized velocity distribution obtained from the three experimental techniques.

Figure 4.17 shows the contour plots of the non-dimensional velocity data from the three experimental techniques. Data from the three experiments are plotted on a scale of 0.1 to 1.4. Figure 4.17a shows the non-dimensional velocity contour plot obtained from the PSV technique. A uniform velocity contour is observed on the

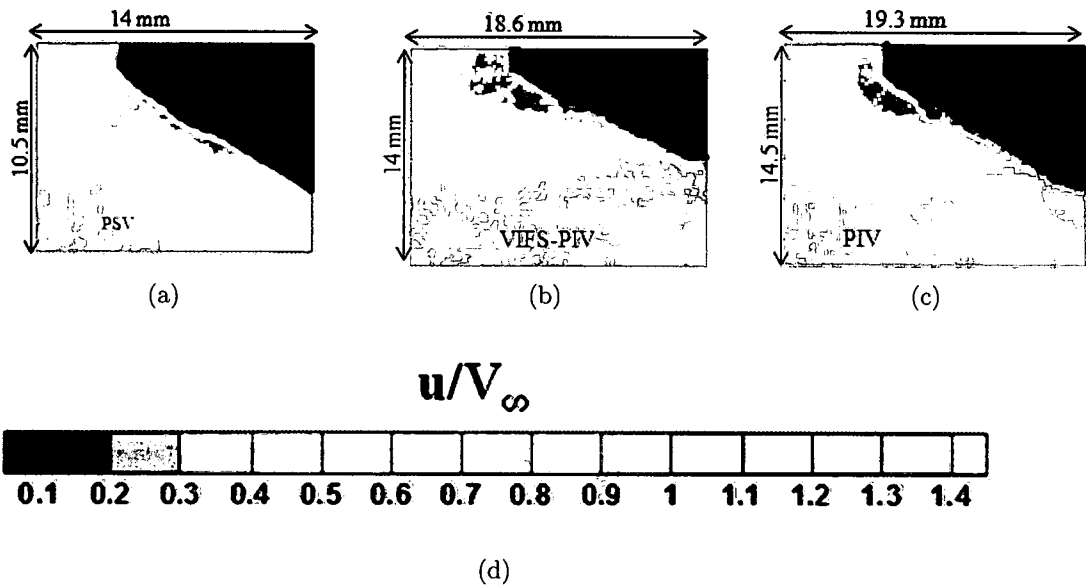


Figure 4.17: Contour plot of the normalized velocity obtained from (a) PSV, (b) VIFS-PIV, and (c) PIV. Image shows the comparison between the velocity data obtained from the three PIVT's.

whole FOV indicating that the seed particles tend to continue the uniform motion of the freestream due to the dominant inertial force of the particles. In Figure 4.17b and c the non-dimensional velocity contours from the VIFS-PIV and PIV techniques are plotted. Both variants of the PIV technique show a gradient in velocity ahead of the probe tip indicating that the flow has a stagnation point near the tip. Due to the limitations in the spatial resolution in the data a stagnation point is not seen in either plot.

Estevadeordal et al studied PSV with cornstarch in 2005. With a FOV of 10 mm they were able to obtain the flowfield data of a uniform flow (Figure 4.18). Physical properties of cornstarch are similar to talc. In the present research data for the uniform flowfield were obtained as expected. In regions where the flow is expected

to curve around the probe, talc's inertia dominated and the obtained data do not represent the flow correctly.

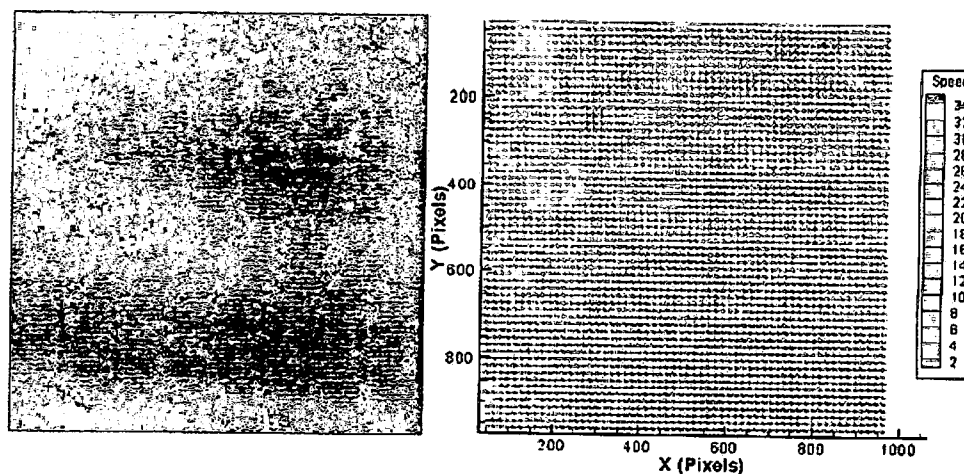


Figure 4.18: Images show an image of a uniform flow seeded with corn starch and the velocity data obtained from a pair of images.[19]

4.7 Validation of the Numerical Investigation

In Figure 4.19, the results from VIFS-PIV, PIV and the computational investigation are shown; the non-dimensional velocity (u/V_∞) contour plots are shown. Though there is a difference in the solution of the VIFS-PIV and the PIV results, a similar contour pattern can be observed. The non-dimensional velocity contour plot from the computational investigation shows a different pattern starting on the surface of the probe. This can be attributed to the change in the wedge half angle of the probe. The probe (Figure 4.20) used in the experimental investigation has a small bump on the surface closer to the tip of the probe.

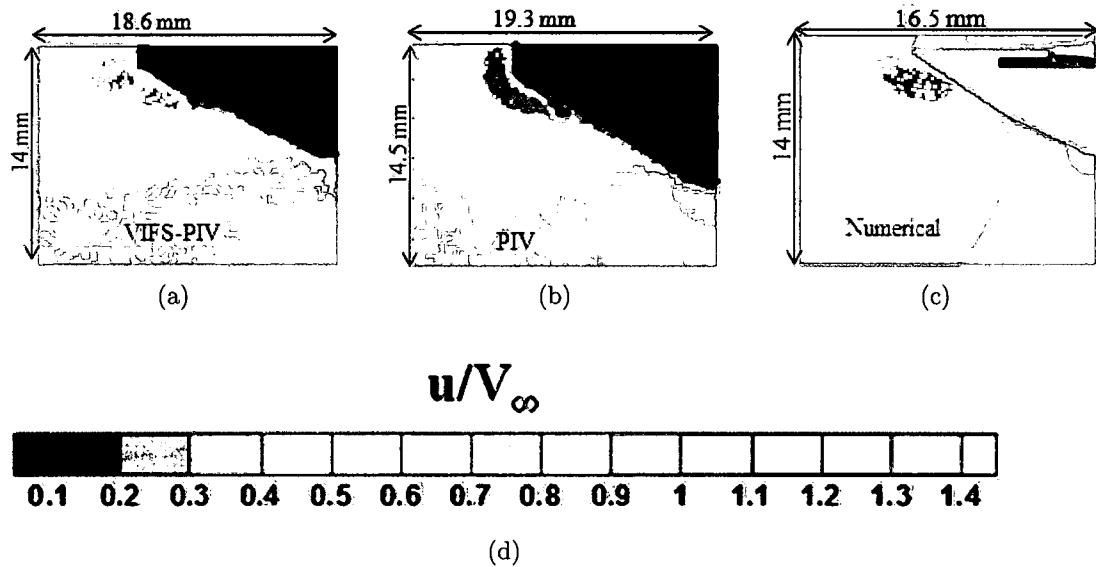


Figure 4.19: Non-dimensional velocity contour plots from (a) VIFS-PIV, (b) PIV and (c) Numerical investigation are shown. All plots are scaled from 0 ~ 1.4. In (c) a different velocity contour from the experiments is observed where the wedge half angle of the model changes.

The boundary of the probe in the captured images may or may not coincide with the interrogation region in the analysis. DPIV analysis of the data with 32 pixel interrogation region and 75% overlap of the neighboring interrogations regions results in an 8 pixel uncertainty in the results.

Figure 4.21 compares the velocity along the radial line 1.5 mm ahead of the probe tip. There is an uncertainty of one interrogation size in measuring the distance ahead of the probe in both variants of PIV. But because the analysis was done with a 75% overlap in interrogation regions this uncertainty is reduced to $1/4_{th}$ interrogation size. Thus the uncertainty in the measured distance in PIV and VIFS PIV are 0.04 mm and 0.09 mm.

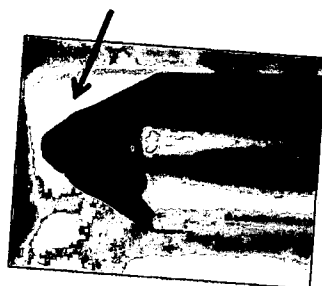


Figure 4.20: Particulate sampling probe highlighting the bump closer to the tip of the probe.

Figure 4.22 shows the percentage difference in the non-dimensional velocity obtained from one method of investigation with the other. The velocity data from the numerical investigation when compared with the velocity data from PIV, a maximum difference of 7% was observed. Similarly, when compared with the VIFS-PIV a maximum of 9% error was observed. The third plot shows the comparison of the VIFS-PIV data with PIV. A maximum 10% difference in velocity data in the two methods is observed. This difference is due to the difference in the spatial resolution obtained from the two methods.

Figure 4.23 shows the non-dimensional velocity comparison of the three investigations. In Figure 4.23, the reference position is at 9.57 mm, which is measured at the end of the conical section of the probe.

In Figure 4.23, data from PIV is consistent, in the region where there is a large velocity gradient the size of the interrogation region is incapable of capturing this gradient and tends to correlate to the lower velocity values. The VIFS-PIV results show a similar trend, but due to a larger interrogation size compared to the PIV data, the velocity is not as resolved as with PIV.

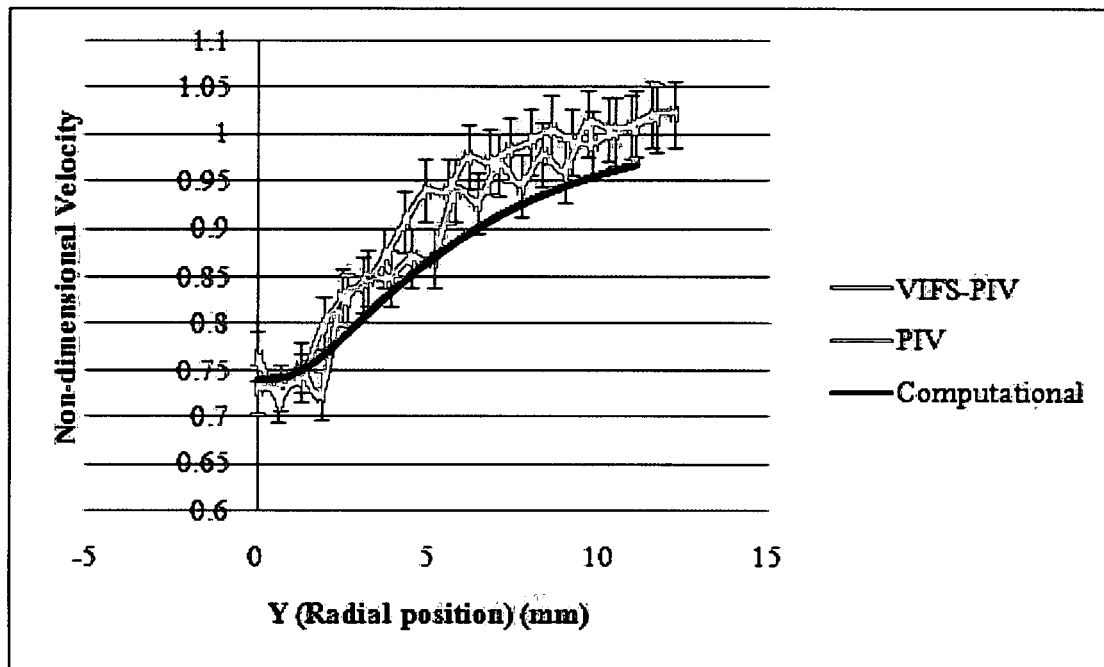


Figure 4.21: Comparison of the non-dimensional velocity plot from the two variants of PIV and the numerical investigation taken 1.5mm ahead of the probe.

The computational results when compared with PIV seem to underpredict the velocity. In the region of high velocity gradient, due to the limitations in the PIV data, the computational results cannot be validated. The approximate maximum thickness of the boundary layer is 0.33 mm and the size of the interrogation region is 0.2 mm. Resolving the boundary layer needs a few interrogation regions inside it.

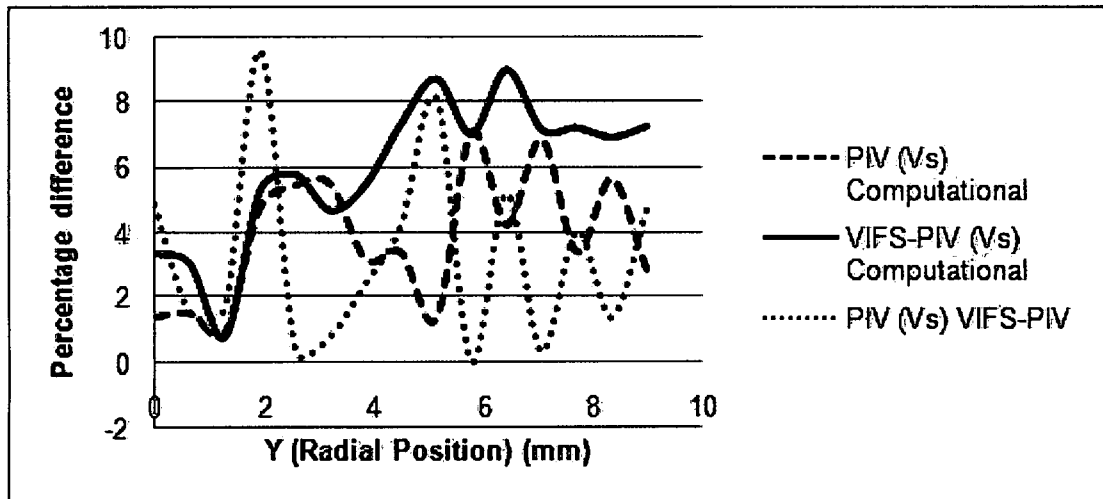


Figure 4.22: Figure shows the percentage difference of the non-dimensional velocity obtained from one method with the other.

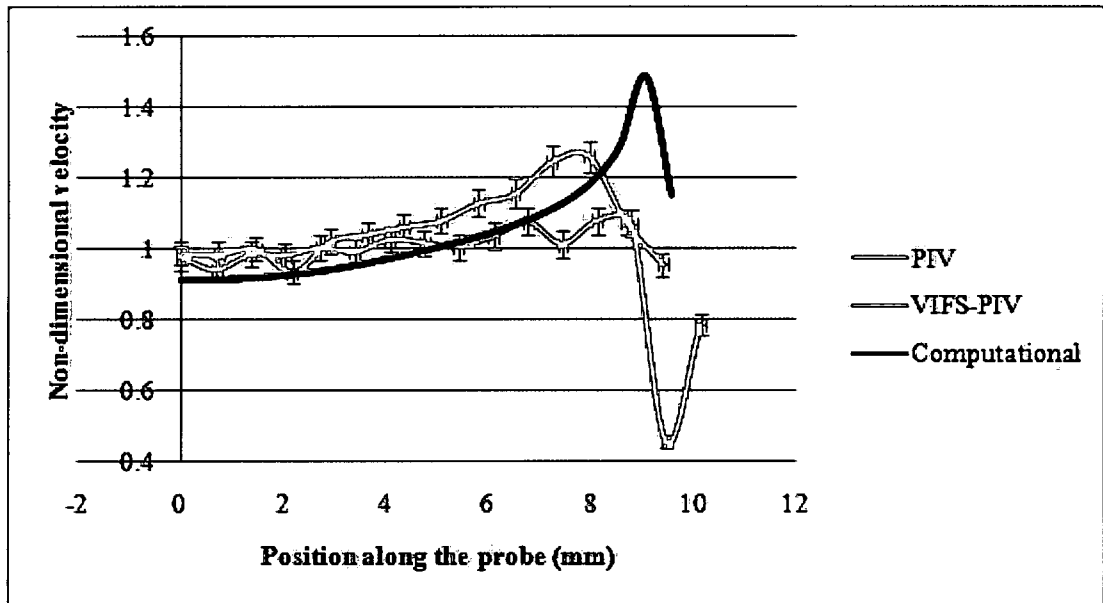


Figure 4.23: Comparison of the non-dimensional velocity plot from the two variants of PIV and the numerical investigation taken 1.5 mm parallel to the probe axis 0.5 mm away from the outer wall of the probe.

Chapter 5

CONCLUSION

The comparative study found the three Particle Image Diagnostic Techniques (PIDT's), Particle Shadow Velocimetry (PSV), Volume Illuminated Forward Scatter Particle Image Velocimetry (VIFS-PIV), and Particle Image Velocimetry (PIV), applicable for near body flow diagnostic study for small Fields Of View (FOV) and Reynolds number 22,000 with respect to the small reference length. Each method was in principle applicable to the problem.

The PIDT's, PSV and VIFS-PIV illuminate the flow volumetrically, whereas PIV uses a thin light sheet for illuminating the flow. Because of the different nature of the experimental setup for each method, the magnification for the experiments varied between 0.61 and 0.85. Particles imaged using the three experimental techniques were 1 ~ 4 pixels in size. A good particle image density was obtained from the three experimental techniques.

From the experiments and discussions, the PSV technique was found to have advantages over the VIFS-PIV and PIV techniques. Because of the incoherent low energy light source used in the PSV experiments there were no reflections from the surface of the model and no speckle pattern was found in the images. In spite of the advantages of the PSV technique, the Stokes number and the response time of the seed material (talc, glass balloons and phenolic resin) used in the PSV experiments were higher than the theoretical constraints to this resulted in the particles not following the flow faithfully. A higher response time and the Stokes number result from the large size (10 - 30 μ m) and high density of the seed material which resulted in dominant

inertia force compared to the buoyancy force. Due to the dominant inertia force, seed particles did not follow the flow faithfully and resulted in biased velocity data. This is not a problem in liquid flows or flows with no accelerations.

Smoke was used to seed the flow in VIFS-PIV and PIV. The Stokes number and the response time for the smoke particles meet the required theoretical constraints.

Though the volume illumination of the VIFS-PIV technique reduced the amount of light reflected from the surface of the model, it also resulted in scattering of light from the out-of-plane particles. The coherent nature of the light formed a speckle pattern due to the light scattered from the out-of-plane particles. The speckle pattern reduced the detectability of the in-plane particles which in turn reduced the spatial resolution.

In PIV, the good seed density gave a 16 pixel resolution which helped to define a highly resolved velocity profile around the particulate sampling probe. PIV gave accurate and more resolved flowfield data compared to VIFS-PIV whereas biased data were obtained from PSV. When utilized properly the three experimental techniques find applicability in flow diagnostics at small FOV and high speed flows.

Results from PIV experiments were used to validate the computational results. For the most part the numerical data closely compared with the experimental data except for the difference in the wedge half angle in the numerical simulation of the data underpredicted the velocity field which results in some variation in the velocity profile.

Chapter 6

RECOMMENDATIONS

The three experimental diagnostic techniques were found to be applicable for flow field diagnostic applications with small Fields Of View (FOV) and high speed flow ($Re = 22000$ with respect to the small diameter of the probe). The limitations observed were due to the implementation of the method than the method itself.

The applicability of the PSV technique can be increased either by using seed material with lower density or using a higher resolution camera (for example a camera with 4 MP array) with the flow seeded with smoke. Similarly the VIFS-PIV technique can be used if the position of the smoke flow in the test section is controlled with a reduced fog. The flow of the smoke inside the test section can be controlled by using honeycomb in front of the test section. This will reduce the amount of smoke in the out-of-plane region reducing the amount of speckle pattern in the images.

Comparing the three PIDT's, if a high resolution camera is employed with the flow seeded with smoke for the tests then PSV has the most advantages and is the best method. Because of the low energy light source the danger of damaging the camera is greatly reduced and the health hazards associated with the laser light source are eliminated. This property can be used to make this a classroom experimental setup for a better aerodynamic understanding of the students. If the LED light source is used then the setup cost for the experiments is greatly reduced. The high repeatability of the LED lights can be used for testing high speed (ex. transonic) flows. The inline illumination the method makes it a simple experimental setup with no complications and synchronizing and the light source is also simple.

BIBLIOGRAPHY

- [1] Briones, A. M., Stouffer, S., Altman, A., Kang, H., Bichal, A., Corporan, E., Belovich, V., "Performance of a Particulate Sampling Probe with Diluter under Gas-Turbine.
- [2] Anderson, J. D. Jr., "Fundamental of Aerodynamics", 4th edition, McGraw-Hill, New York, NY, USA, 2007.
- [3] White, F. M., "Viscous Fluid Flow", 3rd edition, McGraw Hill , New York, NY, USA, 2007.
- [4] Prasad, A. K., "Particle Image Velocimetry", Current Science, Vol. 79, No. 1, 10 July 2000.
- [5] Kompenhans, J., The 12th International Symposium on Flow Visualization, Journal of Visualization, Vol. 10, No. 1, 2007, pp. 123-128.
- [6] Raffel, M., Willert, C., Kompenhans, J., "Particle Image Velocimetry: A Practical Guide", edited by R. J. Adrian, M. Gharib, W. Merzkirch, D. Rockwell, J. H. Whitelaw, Srpinge-Verlag, Berlin Heidelberg, Germany, 1998.
- [7] Westerweel, J., "Digital Particle Image Velocimetry: Theory and application", Delft University Press, Delft, The Netherlands, 1993.
- [8] Adrian, R. J., "Statistical Properties of Particle Image Velocimetry Measurements in Turbulent Flow. In Laser Anemometry in Fluid Mechanics - III (ed. R. J. Adrian) LADOAN Intsituto Superior Technico, Lisbon, pp. 115-129.
- [9] Keane, R. D., Adrian, R. J., "Optimization of Particle Image Velocimeters Part I: Double Pulsed Systems", Measurement Science and Technology, pp. 1202-1215, 1990.
- [10] Keane, R. D., Adrian, R. J., "Optimization of Particle Image Velocimeters Part II: Multiple Pulsed Systems", Measurement Science and Technology, pp. 963-974, 1991.
- [11] Cho, Y. C., "Digital Image Velocimetry", Applied Optics, Volume 28., February 15 1989.

- [12] Keane, R. D., Adrian, R. J., "Theory of cross-correlation analysis of PIV images", *Applied Scientific Research*, Vol. 49, pp. 191-215, 1992.
- [13] Keane, R. D., Adrian, R. J., Zhang, Y., "Super-Resolution Particle Image Velocimetry", *Measurement Science and Technology*, 6, pp. 754-768, 1995.
- [14] Santiago, J. G., Wereley, S. T., Meinhart, C. D., Beebe, D. J., Adrain, R. J., "A Particle Image Velocimetry System for Microfluidics", *Experiments in Fluids*, 25, pp. 316-319, Springer-Verlag, 1998.
- [15] Meinhart, C. D., Wereley, S. T., Santiago, J. G., "PIV Measurements of a microchannel flow", *Experiments in Fluids*, 27, pp. 414-419, Springer-Verlag, 1999.
- [16] Meinhart, C.D., Wereley, S. T., Gray, M. H. B., "Volume Illumination for Two-Dimensional Particle image Velocimetry", *Measurement Science Technology*, 11, pp 809-814, 2000.
- [17] Olsen, M. G., Adrian, R. J., "Out-of-focus Effects on Particle Image Visibility and Correlation in Microscopic Particle Image Velocimetry", *Experiments in Fluids [Suppl.]*, pp. S166 - S174, Springer-Verlag, 2000.
- [18] Chetelat, O., Kim, K. C., "Miniature Particle Image Velocimetry System with LED In-line Illumination", *Measurement Science and Technology*, 13, pp. 1006-1013, 2002.
- [19] Estevadeordal, J., Goss, L., "An Investigation of Particle-Shadow Velocimetry (PSV) for Transonic-Flow Applications", 35th AIAA Fluid Dynamics Conference and Exhibit, 6-9 June 2005, Toronto, Ontario Canada.
- [20] Meksyn, D., "New Methods in Laminar Boundary-Layer Theory", Pergamon Press Inc., New York, NY, USA, 1961.
- [21] Adrian, R. J., "Particle Imaging Techniques for Experimental Fluid Mechanics", *Annual Review of Fluid Mechanics*, Vol. 23, pp. 261-304, 1991.
- [22] Cox, A. J., DeWeerd, A. J., Linden, J., "An Experiment to Measure Mie and Rayleigh Total Scattering Cross Sections", *American Association of Physics Teachers*, 2002.
- [23] Estevadeordal, J., "email communication", Innovative Scientific Solutions, Incorporated, April 08, 2008.
- [24] Crowe, C., Sommerfeld, M., Tsuji, Y., "Mutiphase Flows with Droplets and Particles", CRC press, Boca Raton, Florida, USA, 1998.

- [25] Wen, C. S., "The Fundamentals of Aerosol Dynamics", World Scientific Publishing Co. Pte. Ltd., Singapore, 1996.
- [26] Friedlander, S.K., "Smoke, Dust and Haze: Fundamentals of Aerosol Dynamics", 2 nd ed., Oxford University Press, New York, USA, 2000, Chap. 4.
- [27] Asher, H., "Photographic Principles and Practices", 2nd edition, American Photographic Book Publishing Co., Inc., Garden City, New York, USA, 1975.
- [28] Swedlund, C., Swedlund, E. Y., "Photography: A Handbook of History, Materials and Process", 2nd edition, Holt, Rinehart and Winston, New York, USA, 1981.
- [29] Innovative Scientific Solutions, Incorporated DPIV manual..

R002594240